

# Important Notice

This copy may be used only for the purposes of research and private study, and any use of the copy for a purpose other than research or private study may require the authorization of the copyright owner of the work in question. Responsibility regarding questions of copyright that may arise in the use of this copy is assumed by the recipient.

UNIVERSITY OF CALGARY

A Comparison of Inversion techniques for Estimating VP/VS from 3C3D Seismic Data

by

Paul Fyfe Anderson

A THESIS

SUBMITTED TO THE FACULTY OF GRADUATE STUDIES  
IN PARTIAL FULFILMENT OF THE REQUIREMENTS FOR THE  
DEGREE OF MASTER OF SCIENCE

DEPARTMENT OF GEOSCIENCE

CALGARY, ALBERTA

AUGUST, 2010

© PAUL FYFE ANDERSON 2010

UNIVERSITY OF CALGARY  
FACULTY OF GRADUATE STUDIES

The undersigned certify that they have read, and recommend to the Faculty of Graduate Studies for acceptance, a thesis entitled "A COMPARISON OF INVERSION TECHNIQUES FOR ESTIMATING VP/VS FROM 3C3D SEISMIC DATA" submitted by PAUL FYFE ANDERSON in partial fulfilment of the requirements of the degree of MASTERS OF SCIENCE.

---

*Supervisor, Laurence Lines, Department of Geoscience*

---

*Gary Margrave, Department of Geoscience*

---

*Harvey Yarranton, Department of Chemical and Petroleum  
Engineering*

---

*7 June 2010*

## Abstract

Exploration and development geophysicists regularly make use of prestack analysis of seismic data in order to identify hydrocarbon accumulations in the subsurface in quantities that are economic and in reservoirs that can produce the hydrocarbons efficiently. One commonly used attribute derived from prestack analysis is the ratio of P-wave and S-wave velocities, or  $V_p/V_s$ , however there are a variety of methods available to derive these parameters. This thesis compares three established workflows for estimating  $V_p/V_s$  from 3C3D seismic data, and discusses some of the limitations of each method on both a synthetic model and an acquired 3C3D seismic survey from eastern Alberta, Canada.

The first method is a two step inversion where we first invert for P- and S-wave reflectivity from prestack PP gathers, followed by a second, decoupled inversion of these reflectivities to impedances. Another method condenses this into a single inversion, allowing estimation of P- and S-Impedance directly from prestack PP gathers. The third inversion is similar, in that it is a single-step inversion, however it also incorporates converted wave, or PS, data in an attempt to better constrain the solution by providing additional independent input.

Analysis of the model data has shown that the prestack inversion with converted wave data provides the most accurate estimates of  $V_p/V_s$  of the three methods compared, though the prestack inversion without converted wave data also appears to have far outperformed the two-step inversion in the zone of interest. However the model example also shows a high degree of sensitivity to the registration of the converted wave data to

PP-time and that even small errors in this registration can degrade the quality of the inverted result.

In the case of the real seismic data from eastern Alberta, the prestack inversion without converted wave data has produced the most accurate estimate of  $V_p/V_s$  ratio in the reservoir interval. Interestingly it has been revealed that the two-step inversion process has actually created noise in the  $V_p/V_s$  volume resulting from the de-coupled second inversion step. Correlations to well logs at well locations indicate that the prestack inversion with converted wave data has outperformed the two-step inversion, despite the registration errors that are inherent in the model resulting from an isotropic assumption made in the processing of the converted wave data, which has significantly affected not only the registration of the converted wave data to P-wave time, but has also degraded the bandwidth and amplitude fidelity of the converted wave volumes.

### **Acknowledgements**

Special thanks to the staff at VGS Seismic and Apache Corporation for providing the data and encouragement to continue pushing this data volume to its limits, specifically to Dr. David Monk and Ron Larson. I also thank CGGVeritas Hampson-Russell for software support and extensive code debugging for the joint prestack inversion presented above, especially to Janusz Peron, Keith Hirsche and Graham Carter. To Dan Hampson, as well, who has graciously helped me to understand the concepts behind the inversion engines discussed herein, and to my supervisor Dr. Larry Lines who has provided invaluable support in aiding my transition from industry to academia and provided significant advise in the editing of several drafts of this work. Most especially, thank you to my wife and kids for their love, encouragement and support throughout my return to school.

### **Dedication**

This work is dedicated to my loving family for their continued love and support throughout my education. Elizabeth, Kayla, Andrew, Sianna and Jayden; I could not have done this without your love and support. To my father, Kenneth E. Anderson, who helped me realize I can be more than I am.

## Table of Contents

Approval Page.....	ii
Abstract .....	2
Acknowledgements.....	4
Dedication .....	5
Table of Contents .....	6
List of Tables .....	7
List of Figures and Illustrations .....	8
List of Symbols, Abbreviations and Nomenclature .....	13
CHAPTER ONE: INTRODUCTION.....	18
1.1 Background.....	18
1.2 Literary review.....	24
1.3 Software used.....	26
1.4 Geologic background.....	27
CHAPTER TWO: COMPARISONS OF INVERSIONS ON MODEL DATA .....	31
2.1 Model generation .....	31
2.2 AVO + poststack inversion method on P-wave synthetic data.....	39
2.3 Prestack inversion with P-wave synthetic data.....	44
2.4 Prestack inversion with P-wave and converted-wave synthetic data.....	49
2.2 Discussion – inversions of synthetic data.....	51
CHAPTER THREE: INVERSIONS COMPARISONS OF REAL SEISMIC DATA.....	58
3.1 AVO + poststack inversion method on P-wave seismic data .....	58
3.2 Prestack inversion with P-wave seismic data .....	63
3.3 Prestack inversion with P-wave and converted-wave seismic data.....	69
3.4 Discussion – seismic data .....	72
CHAPTER FOUR: CONCLUSIONS .....	79
CHAPTER FIVE: REFERENCES.....	83
APPENDIX A: PP SEISMIC DATA PROCESSING FLOW.....	87
APPENDIX B: PS SEISMIC DATA PROCESSING FLOW .....	89

**List of Tables**

Table 1: Poststack inversion parameters.....	61
Table 2: Prestack inversion parameters. The terms “ $k_c$ ”, “ $k$ ”, “ $m_c$ ” and “ $m$ ” refer to the slope and intercept of the best fit lines for the cross-plots shown in Figure 8.2.....	64

## List of Figures and Illustrations

Figure 1.1: A comparison of the three workflows compared in this study.....	23
Figure 1.2: Map of portion of 3C-3D volume with wells identified. Wells A, C, D and E have dipole sonic log measurements and Well F has a Vp/Vs log derived from a 3C-VSP experiment. The area shown is approximately 6 miles by 15 miles.....	24
Figure 1.3: Map of Western Canada identifying location of 3C3D program with blue circle (adapted from <a href="http://www.ags.gov.ab.ca/graphics/atlas/fg17_06.jpg">http://www.ags.gov.ab.ca/graphics/atlas/fg17_06.jpg</a> ). .....	27
Figure 1.4: Table of Formations spanning the Mannville and Colorado age deposits of East-Central Alberta. Target formation of this study area are Rex channel sands. Image provided by Energy Resources Conservation Board (adapted from <a href="http://www.ercb.ca/docs/products/catalog/TOF.pdf">http://www.ercb.ca/docs/products/catalog/TOF.pdf</a> ).....	28
Figure 1.5: Cartoon cross-section of Rex channel in relation to lateral and top seals. Note differential compaction characteristic of the channel sands as compared to the regional shaley Rex (adapted from Larson and Anderson, 2006).....	29
Figure 1.6: The Yukon River in Alaska, USA forms a modern analogue for the Rex reservoir sands. Dark meanders indicate shale/silt rich bar deposits where as white indicates either water or sand-rich deposits (from <a href="http://disc.sci.gsfc.nasa.gov/geomorphology/GEO_4/GEO_PLATE_F-12.shtml">http://disc.sci.gsfc.nasa.gov/geomorphology/GEO_4/GEO_PLATE_F-12.shtml</a> ) ..	30
Figure 2.1: Well logs used for generating PP- and PS synthetic gathers used for inversion of model traces. Left synthetic is the PP-gather (0°-30°) and the right synthetic is the PS-gather (0°-30°). Red arrow indicates zone of interest below the coals. ....	32
Figure 2.2: Correlation of logs to P-wave data and to converted-wave data allows identification of key horizons in both domains. Scales for the wells logs are: 480-170 $\mu$ s/m (Vp), 500-3000m/s (Vs), 1.0-3.0 g/cc ( $\rho$ ), 0-0.5 ( $\sigma$ ), 1-150 API (GR), -30 - +90 mV (SP). The resistivity log is on a logarithmic scale from 1-100 ohm-m. ....	34
Figure 2.3: Vp/Vs from horizon-based registration as colour background with PS-data displayed in PP-time (left axis). Horizon lines shown in blue from top to bottom include Base Fish Scales, Viking, Rex Coal, and a deep marker. Sonic log from well D is shown.....	36
Figure 2.4: P-wave velocity from background model used for prestack inversion and the joint prestack inversion. Horizon lines shown in blue from top to bottom include Base Fish Scales, Viking, Rex Coal, and a deep marker. Sonic log from well D is shown.....	36

- Figure 2.5: Comparison of wavelets used for synthetic gather creation. Wavelets are: PP in PP-time (a), PS in PS-time (b), PS in PP-time (c). Note frequency content increase in PS-wavelet when converting to PP-time. Registration of wavelet was done using the Vp/Vs of the zone of interest. .... 38
- Figure 2.6: Comparison of Vp/Vs from logs (green) and AVO + Poststack Inversion (blue). Zone of interest is between 750 and 770 ms. Note that the inverted trace shows good agreement with the log except between 760 – 795 ms, which includes the zone of interest. .... 44
- Figure 2.7: Comparison of Vp/Vs from logs (green) and prestack inversion (blue). Zone of interest is between 750 and 770 ms. Note the improved correlation to the log over the zone of interest as compared to figure 2.6. .... 48
- Figure 2.8: Comparison of Vp/Vs from logs (green) and Joint Prestack Inversion (red). Zone of interest is between 750 and 770 ms. Note the improvement in the correlation to the log trace over the entire trace interval displayed including the zone of interest. .... 51
- Figure 2.9: Correlations between Vp/Vs from well logs with estimates from the various inversion methods with both long (312 ms) and short (73 ms) correlation windows around the zone of interest. All prestack inversion methods (PSI, JPSI, JPSI+HBR) appear to be significantly better in the zone of interest (short window). .... 52
- Figure 2.10: Comparison of the three inversion methods against well control. Track 1 shows the Vp/Vs from well log data, track 2 shows Vp/Vs from AVO + poststack inversion of the model gather. Track 3 shows the Vp/Vs of the well logs which have been corrected by the time-depth relationship derived from correlation with both the PP and PS seismic data. Track 4 is the Vp/Vs ratio from prestack inversion and track 5 is a duplicate of track 1. Track 6 shows the Vp/Vs from the joint prestack inversion, while track 7 is a duplicate of track 3. .... 53
- Figure 2.11: Well log Vp/Vs (black) compared to the AVO + poststack inversion (red), prestack inversion (blue), and joint prestack inversion (green). Note that all prestack inversion methods correlate better over the zone of interest (740 ms – 780 ms) than the AVO + poststack inversion technique. .... 55
- Figure 2.12: Comparison of Joint Prestack Inversion results using different registration methods. Green = logs, Red = Joint Prestack Inversion (JPSI), Blue = Joint Prestack Inversion with Horizon Based Registration (JPSI+HBR). Results are in good agreement above the zone of interest, however amplitude and/or phase distortions are apparent within the zone of interest (740 – 780 ms). Registration time difference is approximately 1 ms (1 sample). .... 57

- Figure 3.1: Prestack P-wave seismic data. Angles are displayed as colour background. Target zone has a maximum angle slightly above  $30^\circ$  ..... 58
- Figure 3.2: AVO attributes  $R_P$  (top) and  $R_S$  (bottom). For location reference, the sonic log from Well F is shown as the red trace in the displays. Key horizons are identified by blue lines. The zone of interest is at approximately 925 ms, immediately below the “Rex Coal” horizon. The lateral extent of the section displayed is approximately 4.1 km (2.57 miles) long. .... 59
- Figure 3.3: P-wave synthetic to seismic well tie for well D. The blue wiggle trace is the synthetic and the red wiggle trace is the seismic data at the well location. Correlation is 69%. .... 60
- Figure 3.4: P-wave synthetic correlations to seismic data at four wells, indicating reasonable quality well ties. .... 61
- Figure 3.5:  $V_p/V_s$  from AVO + poststack inversion.  $V_p/V_s$  from logs at Well D has been inserted in color and the SP log as the trace. .... 62
- Figure 3.6: 7-fold ( $0^\circ$ - $35^\circ$ ) angle gathers from around Well F. .... 63
- Figure 3.7: Well log cross-plots to establish relationships ( $L_P$  vs.  $L_S$  and  $L_P$  vs.  $L_D$ ) for the background model. The left image is a cross-plot of the natural log of P-Impedance versus the natural log of S-Impedance. The right image is a similar plot of the natural log of P-Impedance versus the natural log of density. The geologic interval covers from the Second White Speckled Shale to the top of the coal sequence. Deviations along the vertical axis from the regression lines (red line) correspond to the  $\Delta L_S$  and  $\Delta L_D$  in equations X and X respectively. Large deviations may be indicative of a lithology change. .... 65
- Figure 3.8: Simple 1-layer model showing the exaggerated effect of NMO-stretch on a simple reflector. Note that the same wavelet was used to generate the synthetic at all offsets before normal moveout removal. .... 66
- Figure 3.9: Near (blue) and far (red) angle wavelets used in prestack inversion. In addition to differing frequency content, the average phase of the wavelet is  $26^\circ$  for the near angle and  $54^\circ$  for the far angle. .... 67
- Figure 3.10:  $V_p/V_s$  from prestack inversion.  $V_p/V_s$  from logs at Well D has been inserted in color and the SP log as the trace. .... 68
- Figure 3.11: Near (blue) and far (red) angle wavelets from P-wave data compared to the converted-wave wavelet used in joint prestack inversion. Note that the converted-wave wavelet is significantly lower bandwidth than either P-wave wavelet. The average phase on the converted-wave wavelet is  $-7^\circ$ . .... 70

- Figure 3.12: Vp/Vs from joint prestack inversion. Vp/Vs from logs at Well D has been inserted in colour and the SP log as the trace..... 71
- Figure 3.13: Comparison of Vp/Vs calculated from AVO + poststack inversion (left), prestack inversion (middle) and joint prestack inversion (right). Vp/Vs from logs at Well D has been inserted in color and the SP log as the trace. .... 72
- Figure 3.14: Amplitude spectra of the Vp/Vs volumes taken from 10 inlines around well F. The left image shows the amplitude spectrum from the AVO + poststack inversion has significantly more high frequency noise (red outline) from the inversion than either, the prestack inversion (middle) or the joint prestack inversion (right), and higher frequencies higher than the filter applied to the PP-gathers. Also, the joint prestack inversion does show notches in its spectrum over the converted wave bandwidth (green dashed line). Horizontal axes extends from zero to 150 Hz and the vertical axes from -50 to 0 dB-down. .... 73
- Figure 3.15: Amplitude spectra of the wavelet used in the inversions. The left image shows a comparison of the near angle wavelet (blue) with the wavelet used to invert the P-wave reflectivity (red). A similar comparison is shown for the far angle (blue) and the S-reflectivity wavelet (red). .... 73
- Figure 3.16: Amplitude spectra of the attributes derived from the AVO + poststack inversion flow. The left image shows the spectrum from the P-Impedance, the middle from the S-Impedance, and the spectrum from the Vp/Vs is on the right. Taking the ratio of the impedances has enhanced the high-frequency content of the data, likely by introducing noise. .... 74
- Figure 3.17: Cartoon representation of the idealized (left) and realized (right) boundaries from the independent poststack inversions. The left image shows the idealized case where the bed-boundaries occur coincident on the P- and S-Impedance inversions. The right image shows what has occurred to contribute the high-frequency noise to the resulting Vp/Vs volume, in which the bed-boundaries occur on different samples, resulting in high-frequency jitter imparted to the Vp/Vs volume. .... 75
- Figure 3.18: Detailed trace comparisons for Vp/Vs extracted using on of the three methods discussed above for four wells. The left track shows the Gamma Ray (0-150 API, red), SP (-90 - +30, black) and Density (1.5-3.0 g/cc, blue) logs from the wells where the remaining tracks are comparisons to the various inversions (scale= 1.0 – 3.0) in the order in which they were completed, AVO + poststack inversion, prestack inversion, joint prestack inversion (black=log Vp/Vs, red=inversion, blue=depth-time). The 5<sup>th</sup> track compares each method directly. .... 77
- Figure 3.19: Comparison of the correlation between Vp/Vs from filtered well logs and the various inversion results between the Base Fish Scales (BFS) to the base

of the logs. Note the best results are coming from the prestack inversion (Logs vs. PP). .....	77
Figure 3.20: Plot of well logs for well D. Reflectivity is plotted in the 4 <sup>th</sup> track and shows that the small reflectivity assumption is violated by the coals.....	78
Figure 4.1: Cartoon description of shear-wave splitting. If the mechanism of splitting is aligned along a single azimuth, the time-delay ( $\delta t$ ) can be azimuthally variant (from <a href="http://garnero.asu.edu">http://garnero.asu.edu</a> ). .....	81
Figure 4.2: Example of shear-wave splitting as evidenced on the seismic data used in this study. The left image shows the transverse component of the converted wave data at a single CCP, stacking along different azimuths. The right image shows the same CCP location and the characteristic time delay associated with the fast and slow azimuths. The phase reversals on the transverse section coincides with the fast and slow azimuths on the radial section, providing strong evidence of shear wave splitting. Note that the traveltimes differences of approximately 20 ms shown on the radial data above were not removed prior to stacking, impacting both the amplitudes and frequency content of the radial volume.....	82

### List of Symbols, Abbreviations and Nomenclature

Symbol	Definition
3D	Volume of seismic data that spans 3 spatial dimensions
$\theta$	Angle between a ray and the normal to a reflector
Amplitude	The departure of a wave from baseline (usually zero)
Angle gather	Gather from a common mid point that has been mapped from offset to angle
Asymptotic conversion point (ACP)	Similar to common conversion point, except $V_p/V_s$ is assumed to be constant
AVO	Amplitude Variation with Angle (or offset)
AVOI	AVO + poststack inversion
Bandwidth	The range of coherent frequencies observed in a seismic volume
Bin	Common midpoint
Common conversion point (CCP)	Surface location above where conversion from p-waves to s-waves has occurred
Common midpoint (CMP)	Surface location half way between a shot and receiver
Converted wave	A wave that is emitted at a source as one wave type and reflected as another (e.g. a p-wave is emitted and is reflected back as an s-

	wave).
Density	Mass per unit volume
Dispersion	Variation of velocity with frequency
Gather	A side-by-side display of seismic traces that have some acquisition parameter in common
HBR	Horizon Based Registration
Impedance	Product of velocity and density. Type of impedance refers to the type of velocity used in the calculation (e.g. P-impedance is the product of p-wave velocity and density)
Inversion	Calculation of acoustic impedance from a seismic trace, taken as representing the earth's reflectivity
JPSI	Joint Prestack Inversion (PP+PS)
k	Slope of the linear regression between $L_P$ and $L_S$
$k_c$	Intercept of the linear regression between $L_P$ and $L_S$
$L_D$	Logarithm of Density
$L_P$	Logarithm of P-wave Impedance
$L_S$	Logarithm of S-wave Impedance
m	Slope of the linear regression between $L_P$ and $L_D$

$m_c$	Intercept of the linear regression between $L_P$ and $L_D$
Normal Moveout (NMO)	The difference in the arrival time of a reflection between near and far offsets, usually a parabolic delay
PP seismic data	P-wave (conventional) seismic data
Prewhitening	white noise added to a mathematical process (e.g. inversion) for numerical stability
PS seismic data	Converted wave seismic data (multicomponent)
PSI	P-wave only prestack inversion
Reflectivity	The impedance difference above and below an interface divided by the average of the interfaces
$R_D$	Density Reflectivity
$R_p$	P-wave reflectivity
$R_s$	S-wave reflectivity
Shear sonic	A measurement of the slowness of shear ( $S_v$ or $S_h$ ) waves traveling through a substance (usually a rock body)
Slowness	The inverse of velocity
Sonic	A measurement of the slowness of compressional waves traveling through a

	substance (usually a rock body)
Stationary wavelet	A wavelet that does not vary in time or space
Superbin	A collection of adjacent bins where traces of a common offset range are stacked together
$T_0$	travel time of a wave from a source to reflection and back to the source
Tuning	Interference resulting from two or more reflectors spaced closer than a quarter of the dominant wavelength
$V_{P-ave}$	Average compressional wave velocity between the surface and a reflector
$V_{p-ave}$	Average P-wave velocity, usually calculated from the surface to a reflector
$V_p/V_s$	Ratio of compressional and shear wave velocities
$V_{s-ave}$	Average S-wave velocity, usually calculated from the surface to a reflector
$V_{S-ave}$	Average shear wave velocity between the surface and a reflector
W	A matrix representing the wavelet estimated from seismic data
Well log	A record of measurements made in a borehole

$z$	Depth to a reflection from the surface of the earth
$Z_D$	Density
$Z_P$	P-Impedance
$Z_S$	S-Impedance

## Chapter One: **Introduction**

### **1.1 Background**

The seismic experiment concerns the acquisition, processing and interpretation of seismic waves reflecting and refracting off layers of rock in the subsurface. The two primary types of seismic waves used in reflection seismology are P-waves (also called compressional or longitudinal waves) and S-waves (also called shear or transverse waves). The velocity of these waves is governed by the properties of the substance the waves are traveling through and can be used as an aid to identify rock types and properties without physically sampling the rock. Similarly, the ratio of P-wave to S-wave velocities can not only be a reflection of the lithology of the rock the waves are traveling through, but also the fluid that has saturated the pores of the rock, and even the relative amount of porosity present. For the rocks sampled by local well logs, limestones generally have lower  $V_p/V_s$  than sandstones, which are generally lower than clay-rich shales, for example. While most sound sources for the seismic reflection surveys generate P-waves primarily (e.g. dynamite, air-gun or vibratory), mode conversions occur at every contrast in either P-wave velocity, S-wave velocity, or density, which results in both reflected and transmitted P- and S-waves at each of these interfaces. The ratio of energy that emerges from each of these interfaces is dependant upon the incident angle of the sound energy. Typically all the reflected and transmitted energy for a sound wave incident normal to an interface is also P-waves, however, as the angle changes from normal to parallel, the amount of energy transmitted and reflected as P- and S-waves changes. The most common description to describe this energy partitioning was described by Zoeppritz, building upon work by Knott (Aki and Richards, 1980), often

referred to as the Zoeppritz (or Knott-Zoeppritz) equations. For a wave emitted as a P-wave at the source, traveling at P-wave velocity to an interface, where it is reflected back to the surface where it can be recorded by a geophone, we refer to this reflection as a PP-reflection. Similarly, a P-wave source emitting a wave from the source to a reflection where it is converted to an S-wave and returns to the surface is referred to as a PS-reflection (or converted wave reflection). For most seismic reflection experiments, it is only the reflected energy that is recorded and available for further processing and analysis and it is processing and analysis of these converted waves upon which geophysicists base interpretations of lithology, porosity and fluid content, among other attributes that may be relevant to the rock.

The work that follows is a comparison of three seismic inversion methods for estimating  $V_p/V_s$  of the subsurface from seismic data to determine the rock properties present, in order to identify zones of specific lithology and/or fluid content for mineral or hydrocarbon exploration. Inversion is a general mathematical process which has been adopted for a variety of seismic data problems, including inversion of prestack seismic data for P-wave and S-wave impedance (Lines and Newrick, 2004). In this case, the intent is to produce earth models from available data. The intent, in this example, is to invert reflectivity data for the P- and S-Impedances that gave rise to the reflectivity, however, this is not without problems. Seismic inversion (as with most inversions) is often non-unique, meaning for a given input data volume, there is a vast solution space of equally valid solutions, for a given set of constraints. One way of decreasing this ambiguity is in constraining the solution with additional, independent input. In the case of inverting for impedances, the minimum required input is one sample as in the case of

post-stack inversion. We can constrain this result by including more data with different incident angles, as in prestack inversion. By adding additional data, for example PS-reflectivity, we further constrain the inversion solution as the solution is required to honour multiple datasets, ignoring the potential impact of noise on the input data. This is often called simultaneous inversion (Sheriff, 1991) or joint inversion.

Until recently, inversions of seismic data for impedance (e.g. Lindseth (1979)) were typically poststack inversions of stacked data. Stacked data is comprised of summing seismic data that has been processed and sorted to common midpoints located between the source and receiver locations, to form common midpoint gathers. These gathers are then averaged at each midpoint to produce a single output (i.e. stacked trace) which can then be inverted to P-Impedance. With the popularization of amplitude versus offset (AVO) methods over the past 30 years, inversion was extended to a two step inversion workflow (Goodway et al., 1997). The first inversion uses common midpoint gathers and inverts the amplitudes to P-wave and S-wave reflectivity, using offset dependent reflectivity as described by many authors (e.g. Fatti et al., 1992). The second process involves inverting each of these reflectivity attributes independently following a methodology similar to that of Lindseth (1979).

In recent years, a full prestack inversion has become more popular as computers are now able to manage the computations on vast amounts of input data in useful timeframes. This simplifies the previously mentioned two-step inversion to a single step, from prestack gather to P- and S-Impedances. This also helps to remove some errors that resulted from decoupled P- and S-Impedance inversions, which were independent inversions for a common Earth Model. Because the inversion must now be solved (i.e.

by minimizing solution error) on multiple datasets, in this case multiple offsets at each time sample, the solution for both P- and S-Impedance are constrained by one another. While multicomponent seismic data is not a new concept in literature (Stewart, 1990; Margrave, 2001; Veire and Landro, 2006), its use has been somewhat limited by computer power and software availability for working with it effectively. Similar to prestack inversion, joint prestack inversion is a tool that has recently become more readily available. As a result, it is another dataset that can be included in the inversion process to aid in the estimation of P- and S-Impedance, and should similarly constrain the solution space. Discussed in more detail later, a critical requirement for using converted wave data in a joint prestack inversion, or most other analysis methods, requires that the converted wave data be registered from PS-time to PP-time. With conventional PP seismic data, waves travel through the earth to a reflector and back to the surface all at P-wave velocity. For converted waves however, while the wave does still travel down to the reflector at P-wave velocity, when it is reflected, it returns to the surface at S-wave velocity, which is significantly slower than P-waves (typically approximately to 50%). This means that for a single reflector, the P-wave reflection will be detected before the converted wave reflection. To align geology correctly between P-wave and converted wave data, the converted wave data must be related to the P-wave data, either by depth migration (Stewart, 1990) or by some method of manual event alignment in time domain, as described later in the text.

This thesis examines three types of inversion that employ one of the three methods described above. The performance of these inversion methods is compared for an eastern Alberta data example acquired with digital 3-component (3C) receivers. The

primary targets in this experiment are Mannville-age fluvial channels. While easily identifiable on 3D seismic data, reservoir quality remained an issue which conventional stacked data alone could not further high-grade. It was anticipated that the multicomponent seismic data would provide the leverage necessary to aid in drilling economic gas wells with a higher degree of success as multicomponent data contains more information about the seismic wavefield (i.e. reflections) than conventional single vertical component data alone. Anderson and Larson (2006) showed that such hope appears to have been realized, with look-back drilling success rates improving from 31% with P-wave seismic only, to 65% when integrating the information from the P-wave and converted-wave volumes. Also discussed by Anderson and Larson (2006),  $V_p/V_s$  is related to reservoir quality for the target sands. A project was then undertaken to evaluate the differences in predicting rock properties, specifically  $V_p/V_s$ , from seismic data using one of three paths (also see Figure 1.1):

- Amplitude variation with offset (AVO) analysis followed by poststack inversion of the AVO attributes (AVOI, Goodway et al., 1997)
- Prestack inversion of the P-wave gathers directly to impedances (PSI, Hampson et al., 2005)
- Joint prestack inversion of the P-wave gathers and a converted-wave volume (JPSI, Hampson et al., 2005)

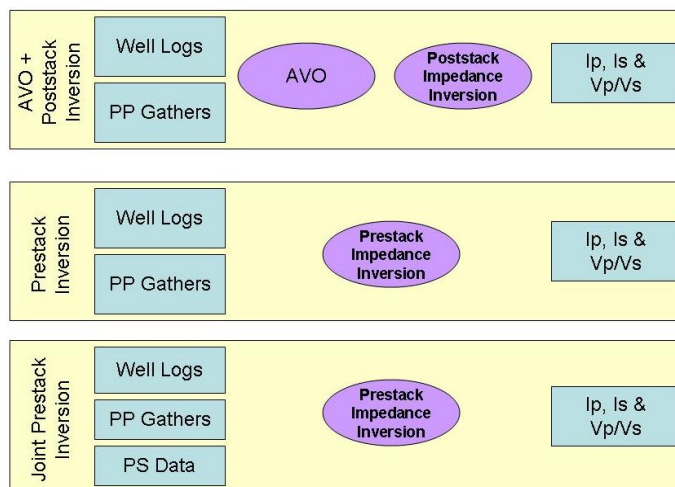


**Figure 1.1: A comparison of the three workflows compared in this study.**

The procedure and results from that analysis are presented below. A map of the seismic data identifying the relative positions of the wells is provided in Figure 1.2. Before discussing the inversions of the acquired seismic data, a comparison of the same inversions applied to synthetic data is first discussed.

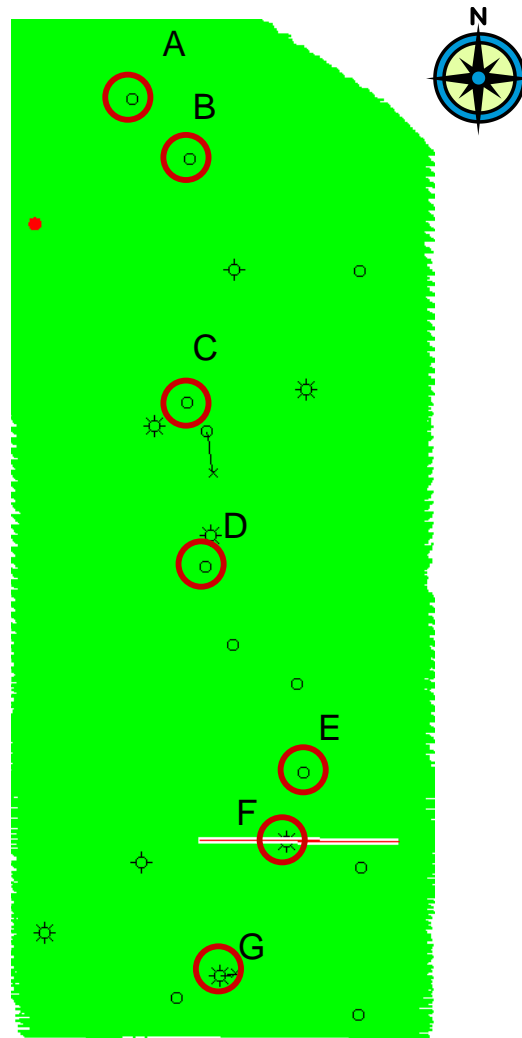


**Figure 1.2: Map of portion of 3C-3D volume with wells identified. Wells A, C, D and E have dipole sonic log measurements and Well F has a Vp/Vs log derived from a 3C-VSP experiment. The area shown is approximately 6 miles by 15 miles.**

## 1.2 Literary review

Various methods for evaluating and interpreting reflection seismic data have been in the works for several decades. Most methods are based upon the equations of Zoeppritz (1907) and Knott (1899), which describes the partition of energy from an incident plane wave impinging upon the boundary between two semi-infinite half-spaces. In general, full use of these equations is impractical in exploration seismology as it

requires the sampling of data which is unobtainable, specifically the recording of waves transmitted through the earth which never return to the surface. As a result, the original Knott-Zoeppritz equations have been simplified, the most common incarnation having been derived by Aki and Richards (1980). This simplification reduced the Knott-Zoeppritz equations from 16 equations with 16 unknowns to a single equation with three unknowns, however this did require some key assumptions to be made. Specifically that reflectivity at any given interface is small and that refractions do not occur.

The work of Aki and Richards has been further expanded upon by a large variety of authors. One approach taken to this analysis was to reformulate the Aki and Richards equations in terms of P-wave and Poisson's Ratio as was popularized by Shuey (1982) and Verm and Hilterman (1995). A second approach following from Aki and Richards continues to define the unknown terms of their equations in terms of P-wave velocity, S-wave velocity, and density. Smith and Gidlow (1987), Gidlow et al. (1992), Fatti et al. (1994), Larsen (1999), and Downton (2005), among others, have proposed various methods and approximations to the Knott-Zoeppritz or Aki and Richards equations. Converted wave seismic data, or PS-data, has also been incorporated into prestack inversion in a variety of ways. Stewart (1990), Larsen (1999) and Margrave et al. (2001), though these are reflectivity, or AVO, inversions and not impedance inversions as discussed in this thesis.

While the above methods do provide a means of estimating rock properties such as facies, fluid content, and porosity, relating reflectivity changes to petrophysical changes can be non-unique (Hilterman et al., 1996). Lindseth (1979) proposed using inverted log data to simulate well logs in order that these parameters might be more

quantitatively determined (Wallace et al., 1996). By inverting the reflection data to impedance, information about individual layers of rock and the changes within each layer can be more quantitatively determined.

The utility of Vp/Vs as an indicator of rock and fluid properties have been demonstrated by Tatham (1982), Freund (1992), Castagna (1985), and Mavko (1998), amongst others. The explorationist is tasked to identify drilling locations over commercially viable quantities of hydrocarbon accumulations from productive reservoirs, which requires information about the rock and fluid properties present. Because 3D seismic data is able to sample large volumes of the subsurface, the ability to convert this information Vp/Vs in order to determine rock and fluid properties can be of great value in identifying viable drilling targets. Work by Goodway et al. (1997), Pendrel (2000), Ma (2002), Young et al. (2005) and others has demonstrated the utility of estimating rock properties from prestack seismic inversion, by effectively combining impedance inversion (Lindseth, 1979) with one of the various AVO methods discussed above. Extending these impedance inversion methods to incorporate converted wave data has been published by a variety of authors, including: Agullo et al. (2004), Knapp et al. (2002), and Hampson et al. (2005).

### **1.3 Software used**

Various software was used to interpret, invert and analyse the tests performed herein. Hampson-Russell software was used for all inversions and AVO analysis on both the synthetic and real seismic data. It was also used to generate the model data used in testing the three inversion methods.

Additional software used included SeisWare for conventional interpretation of the conventional seismic data (i.e. horizon picking) and Microsoft Excel for a variety of the displays and analysis that follows. Image editing was performed using Microsoft Powerpoint and the thesis was compiled and edited using Microsoft Word.

#### 1.4 Geologic background

The 3C3D seismic program and wells being investigated as part of this study are located in east central Alberta, Canada (figure 1.3). The primary geologic target for oil and gas exploration on this 3D seismic program is upper Mannville aged Rex channel sands within a regionally continuous shale Rex member (Figure 1.4). These sand channels tend to be three (3) to ten (10) meters thick, when present, and approximately 200 – 250 meters wide at a depth of approximately 800 meters below the surface. A commercially successful well will yield 0.7 Bcf of gas with initial production rates above 500 mcf/day.

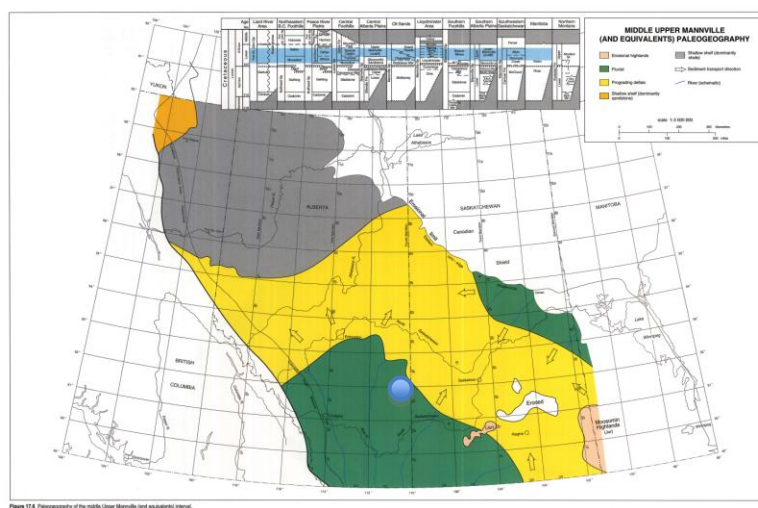


**Figure 1.3: Map of Western Canada identifying location of 3C3D program with blue circle (adapted from [http://www.ags.gov.ab.ca/graphics/atlas/fg17\\_06.jpg](http://www.ags.gov.ab.ca/graphics/atlas/fg17_06.jpg)).**

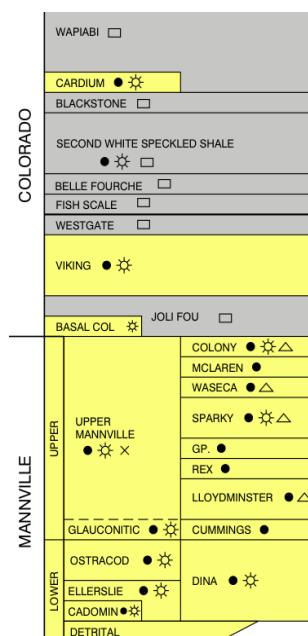


**Figure 1.4: Table of Formations spanning the Mannville and Colorado age deposits of East-Central Alberta. Target formation of this study area are Rex channel sands. Image provided by Energy Resources Conservation Board (adapted from <http://www.ercb.ca/docs/products/catalog/TOF.pdf>)**

While the lateral seal for the channel sand consists of regional shales, the top seal is a regionally continuous Rex-age coal. Similar age coals can also be present laterally, adding complication to the geology of the area. Since coals are typically the remains of ancient swamps, we can infer that the sediments were initially deposited over relatively flat areas with occasional channels cutting throughout. Over geologic time, however, the regional shales compact more under the overburden rocks than the more sandy channels, resulting in differential compaction over the channel sands (Figure 1.5).

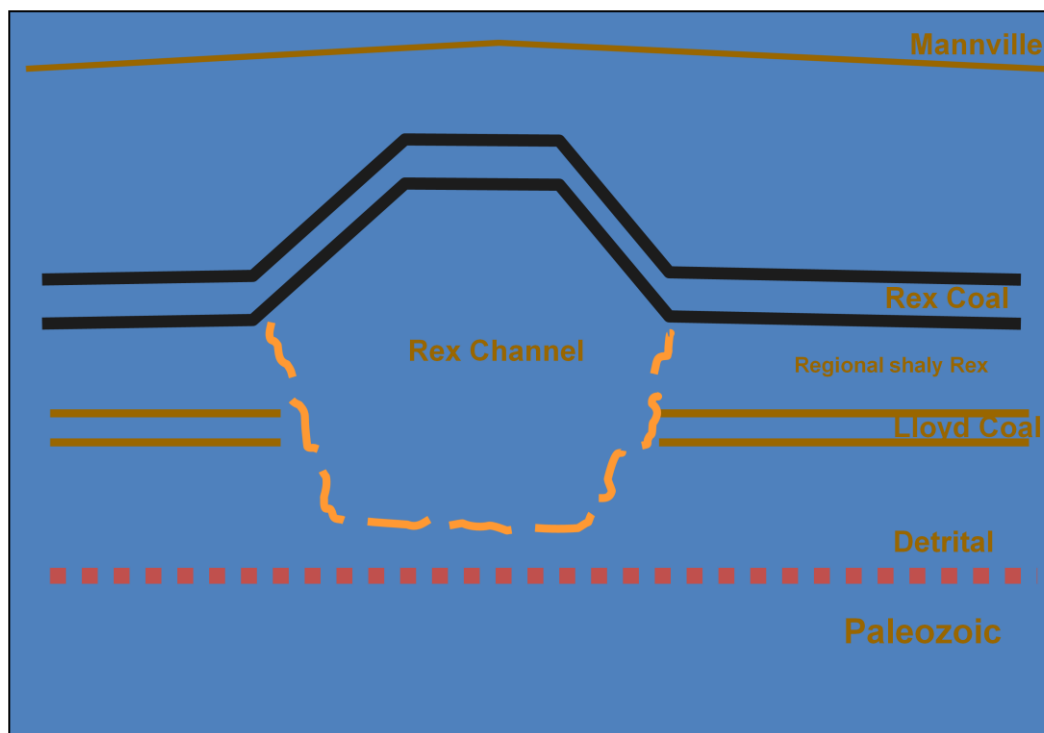


**Figure 1.5: Cartoon cross-section of Rex channel in relation to lateral and top seals. Note differential compaction characteristic of the channel sands as compared to the regional shaley Rex (adapted from Larson and Anderson, 2006).**

In some cases, the pore-throats of the sandy-channels can be plugged by fine grained sediments, resulting in poor reservoir quality. As a result, differential compaction alone cannot accurately predict the presence of reservoir, but only the presence of the channel itself. Figure 1.6 shows a modern river system, which while more energetic than the Rex channels, it does demonstrate the differences in reservoir quality along the river, even within the channel complex itself. The Yukon River in Alaska, USA, shows sandy bars and shale/silt rich bars, within the same channel system only a short distance apart. If the channel contains relatively high shale content, it will not provide economic development due to poor permeability, despite the presence of enough sand to allow for differential compaction.



**Figure 1.6: The Yukon River in Alaska, USA forms a modern analogue for the Rex reservoir sands. Dark meanders indicate shale/silt rich bar deposits where as white indicates either water or sand-rich deposits (from [http://disc.sci.gsfc.nasa.gov/geomorphology/GEO\\_4/GEO\\_PLATE\\_F-12.shtml](http://disc.sci.gsfc.nasa.gov/geomorphology/GEO_4/GEO_PLATE_F-12.shtml))**

## Chapter Two: **Comparisons of inversions on model data**

### **2.1 Model generation**

In order to better understand the differences between the methods, it is worthwhile to first perform the comparison that follows on synthetic data where the correct answer is known. This allows for comparative assessment of the outputs arising from the real seismic data experiment. This also allows for the method to be tested for its general accuracy in a case where the solution is known. Sonic and density well logs from within the seismic data outline (Figure 1.2) were used to create both P-wave and converted-wave PS angle gathers which were then inverted using each of the above-mentioned methods. For the purposes of this experiment, the Knott-Zoeppritz equations were used to derive the synthetic traces. The Knott-Zoeppritz equations describe how energy will partition into reflected and transmitted P- and S-waves, for a wave incident on an interface at a given angle relative to the normal. The Knott-Zoeppritz equations consist of 16 equations with 16 unknowns, and are functions of the velocities above and below the interface in question. These equations have been simplified by many authors, including; Shuey (1983), Verm and Hilterman (1995), and Fatti et al. (1992), as commonly referenced examples in literature.

For both the PP- and PS-synthetic gather, seven angle-traces were created varying between 0 and 30 degrees with a 1-millisecond sample rate (Figure 2.1). In general, the frequency content of signal on converted wave data is typically lower than its PP counterpart (Anderson and Larson, 2006; Stewart, 1990), in their native domains. This was replicated in this synthetic example by using different bandpass wavelets for the PP (5/10 - 80/110 Hz) and PS (2/4 - 30/50 Hz) synthetics. The gathers were then inverted

through three inversion processes; PP-AVO followed by poststack inversion, PP prestack inversion, PP and PS joint prestack inversion. Additionally, because this is synthetic data, the impact of small PP-PS registration errors, described later, can also be tested.

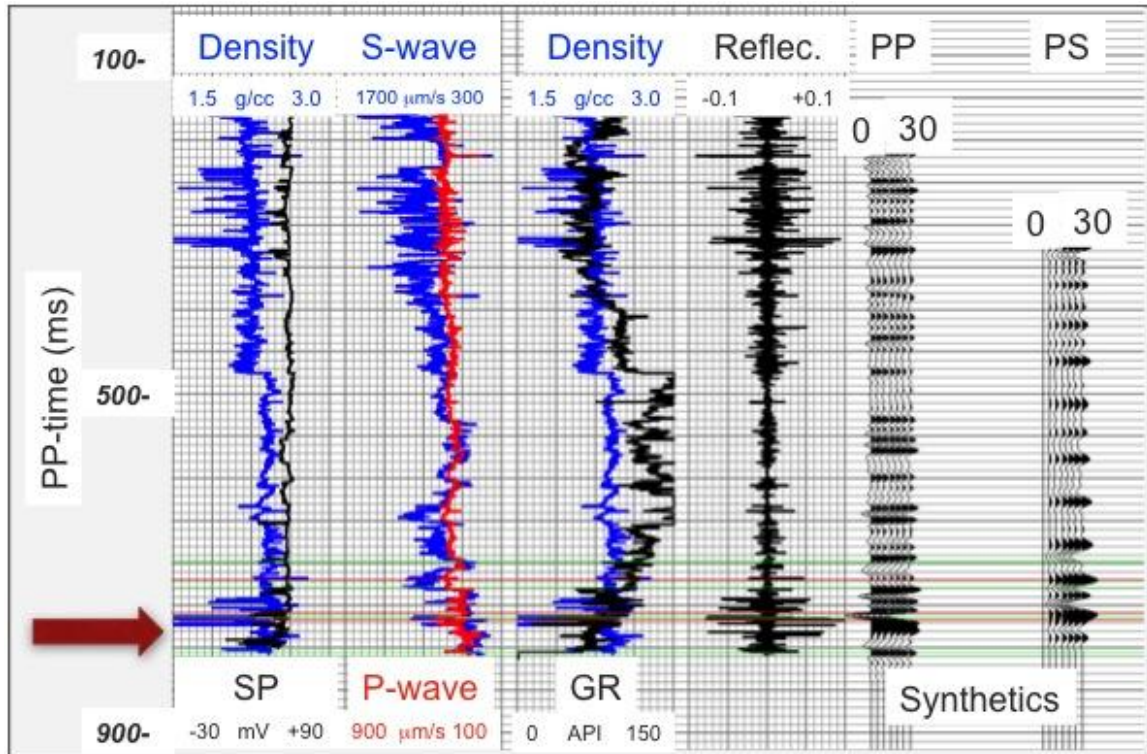


**Figure 2.1: Well logs used for generating PP- and PS synthetic gathers used for inversion of model traces. Left synthetic is the PP-gather (0°-30°) and the right synthetic is the PS-gather (0°-30°). Red arrow indicates zone of interest below the coals.**

Before incorporating the converted-wave information, we must first ensure that all data to be used is in a common domain, as discussed above. The issue is that conventional (P-wave) seismic data is recorded in time, however this is really the time for a P-wave to travel a specified distance to a reflector and back to the surface. In the case of normal moveout corrected P-wave data, this is the  $T_0$ -time given by

$$T_0 = \frac{2z}{V_{P-ave}} \quad (1)$$

where  $V_{P-ave}$  is the average P-wave velocity for a source wavelet to travel from the surface to the reflector, and back again at zero offset. In the case of converted-waves however, this equation must be modified such that we account for the wave traveling down at P-wave velocity and returning at S-wave velocity

$$T_0 = z \left[ \frac{1}{V_{P-ave}} + \frac{1}{V_{S-ave}} \right], \quad (2)$$

where the reflected S-wave returns at the average shear wave velocity ( $V_{S-ave}$ ). This however leads to a difficulty in that we do not explicitly know the S-wave velocity to each event in our seismic section in much the same way we do not know P-wave velocities well enough to produce perfect depth conversions.

The solution is to correlate events of key geologic markers that are regionally consistent and visible on both the P-wave and converted-wave seismic sections. Because we have correlated well logs to P-wave seismic sections, we know where each geologically significant event exists on P-wave gathers, which we can repeat with the converted-wave data. Using the correlated P-wave sonic log and the integrated S-wave sonic log, the software can develop a converted-wave synthetic. We can now correlate the converted-wave synthetic to the converted-wave seismic data following the same procedure used previously for the P-wave data. Given the resulting depth to converted-wave time relationship, we can now identify which geologic events are consistent between the P-wave and converted-wave volumes (Figure 2.2).

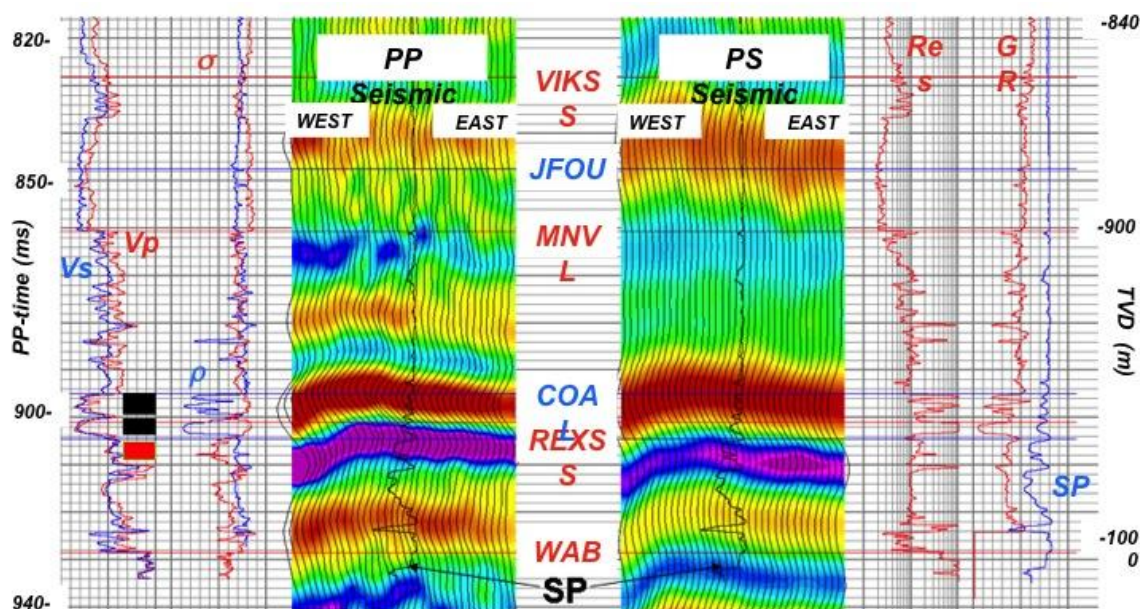


**Figure 2.2: Correlation of logs to P-wave data and to converted-wave data allows identification of key horizons in both domains. Scales for the wells logs are: 480-170  $\mu\text{s/m}$  ( $V_p$ ), 500-3000m/s ( $V_s$ ), 1.0-3.0 g/cc ( $\rho$ ), 0-0.5 ( $\sigma$ ), 1-150 API (GR), -30 - +90 mV (SP). The resistivity log is on a logarithmic scale from 1-100 ohm-m.**

We now have two methods of calculating the  $V_p/V_s$  from the well log data;

1. ratio of the compressional and shear sonic logs, and
2. ratio of the depth-time curves derived by correlating synthetics to the P-wave and converted-wave volumes.

wave and converted-wave volumes.

Differences between these methods may exist due to a variety of factors including dispersion, however they are expected to be relatively consistent with one another. These curves will be compared in a later section. Now that we have the ability to register the data at the wells, we need to extend that throughout the volume. To do that we used the previously mentioned geologic markers that are consistent between the P-wave and converted-wave sections. First we pick these horizons throughout each volume independently. Once that is completed, we can now force the converted-wave horizons

to P-wave time. To do this, we go back to the equations defined above for zero-offset traveltime. When performing the registration in this manner, it is important to watch that the domain-specific reflectivities are accounted for. For example, it is possible that an event used for horizon-based registration is a peak on the P-wave volume (i.e., an impedance increase) but is a trough, zero-crossing or something in between on the converted-wave volume. Such effects will result in registration errors and could result in non-geologic  $V_p/V_s$  being calculated. It is important to ensure that the  $V_p/V_s$  derived from the horizon-based technique is consistent with well control. Figure 2.3 shows the converted-wave data in P-wave time with the background colour defined as the horizon-based  $V_p/V_s$ . The  $V_p/V_s$  calculated from the depth-time curves has been inserted into the section for comparison, in this case it appears to be a fair match. While we are able to use this  $V_p/V_s$  to register the volume to P-wave time, it is worth noting that it has considerably less resolution than is present in the background velocity model used for inversion (Figure 2.4). The geologic horizons used to build the registration  $V_p/V_s$  included the Base Fish Scales (BFS), and the Rex Coal. Attempts were made to use additional horizons, however the different frequency content of the volumes limits our ability to pick consistent geologic events in order to produce geologically realistic  $V_p/V_s$ .

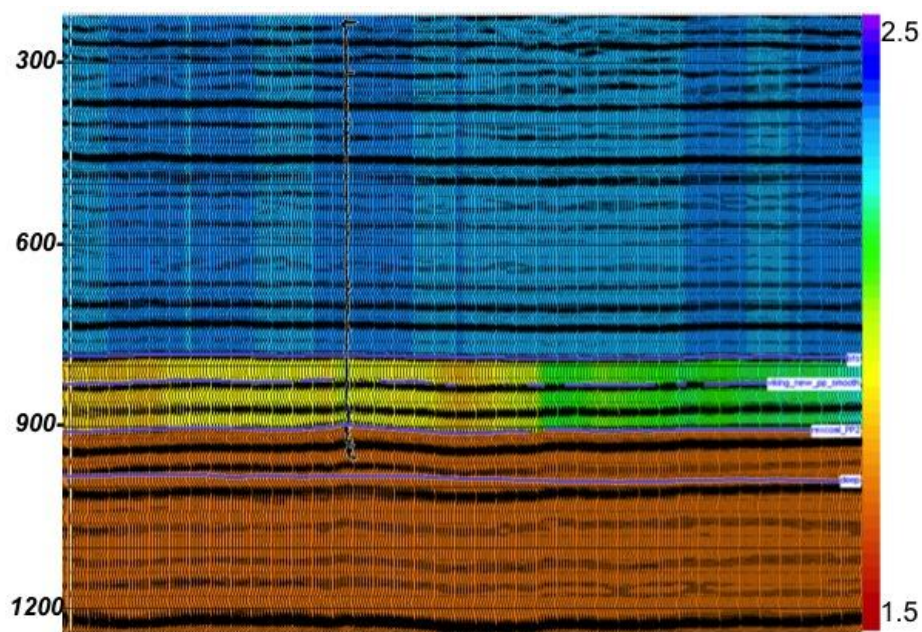


Figure 2.3:  $V_p/V_s$  from horizon-based registration as colour background with PS-data displayed in PP-time (left axis). Horizon lines shown in blue from top to bottom include Base Fish Scales, Viking, Rex Coal, and a deep marker. Sonic log from well D is shown.

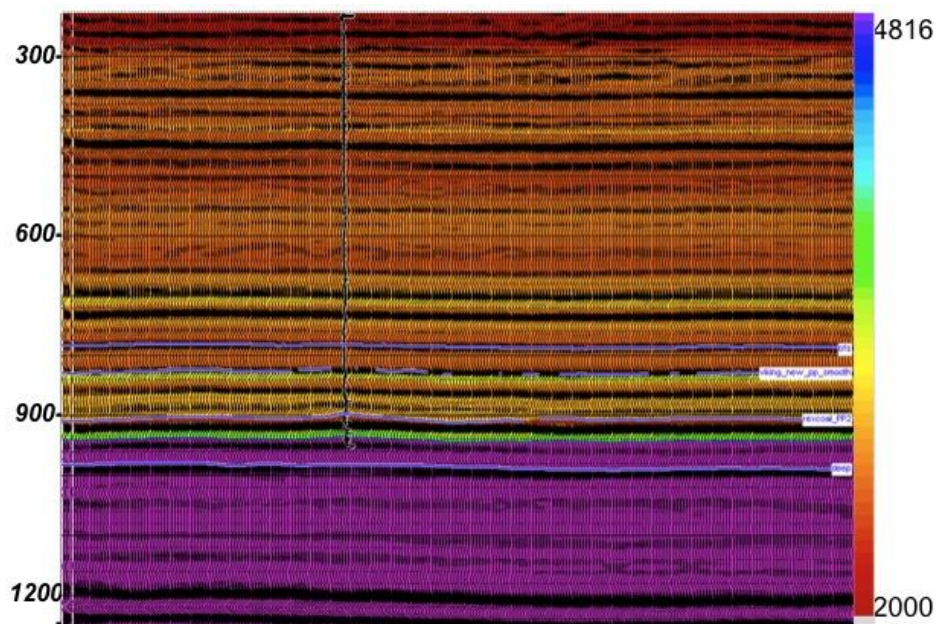


Figure 2.4: P-wave velocity from background model used for prestack inversion and the joint prestack inversion. Horizon lines shown in blue from top to bottom include Base Fish Scales, Viking, Rex Coal, and a deep marker. Sonic log from well D is shown.

The vertical resolution of the  $V_p/V_s$  volume from registration is often too low to be of value in determining the rock properties of potential reservoir formations, because the velocities used in equation (2) are average velocities over geologically large intervals. As an aside, while not incorporated into the software at this time, there could be additional value in incorporating this registration  $V_p/V_s$  volume as a soft-constraint into the inversion. At this time, it is only used to register the converted-wave data to P-wave time.

The synthetic gathers are generated using the  $V_p/V_s$  of the model, meaning that the correct registration is known and defined by the sonic well log data. It is important to know that this is only true in the case of a model dataset as in reality the correct  $V_p/V_s$  for registration cannot be known. In order to simulate the workflow used on real seismic data, manual registration of the same synthetic PS-gather was also performed, resulting in a slightly different registration, in order to determine what, if any, impact registration errors could have on joint prestack inversion. This is an important factor to understand in order to determine if the level of accuracy and detail required to properly perform a joint prestack inversion has been achieved or if additional processing steps and/or additional horizons for registration may be necessary.

Because the inversion is now including the PS angle gather, a corresponding wavelet is required in order to properly represent the signal bandwidth of the gather. Typically, a wavelet is extracted from the corresponding data after registering the data to PP-time as the inversion is performed in that domain, however in this case, the wavelet used for generating the synthetic was compressed to PP-time using the  $V_p/V_s$  of the

model around the zone of interest. Figure 2.5 shows a time and frequency domain comparison of the wavelet in both its native PS-time and in PP-times.

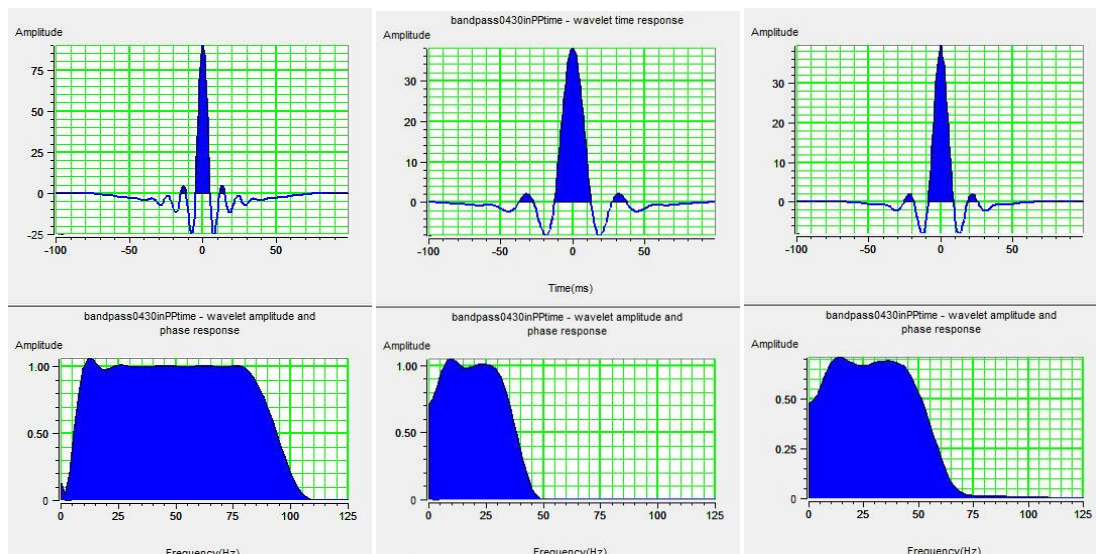


**Figure 2.5: Comparison of wavelets used for synthetic gather creation. Wavelets are: PP in PP-time (a), PS in PS-time (b), PS in PP-time (c). Note frequency content increase in PS-wavelet when converting to PP-time. Registration of wavelet was done using the  $V_p/V_s$  of the zone of interest.**

One consequence of the different, and usually lower, frequency content of the converted-wave data is in temporal resolution of the data. Seismic data is assumed to be a band-limited reflectivity series. By limiting the bandwidth of the data at high frequencies, the data is no longer able to resolve reflectors above a given thickness. As a result, tuning will often manifest itself on all seismic data, however in this example, the converted wave data is impacted to a higher degree due to its inherent lower bandwidth, which increases the tuning thickness significantly, in this case. Widess (1973) and others have discussed the difficulties encountered when interpreting amplitudes from bandlimited reflectivity. The problem is that as two reflections get closer together, the waveforms representing each reflection get close enough that they can not only begin to

distort one another, affecting the amplitude fidelity of each reflection. The result is that the input data amplitudes have been corrupted by tuning and are not representative of the reflectivity of a series of distinct interfaces, but rather an averaged reflectivity series, which can predictably have an impact on amplitude inversion for impedance.

Both joint inversions were completed using the same general parameters used in the previous inversions, for consistency. These inversion results will be discussed in more detail in the following section.

## 2.2 AVO + poststack inversion method on P-wave synthetic data

The process of estimating  $V_p/V_s$  with a poststack inversion method follows the procedure outlined by Goodway et al. (1997) and described in the upper flow-chart of Figure 1.1. In their paper, Goodway et al. propose starting with prestack single-component data ( $S(\theta)$ ) and performing an amplitude variation with offset (AVO) inversion of these gathers, in order to estimate the P-wave and S-wave reflectivities,  $R_p$  and  $R_s$  respectively. One such method is an approximation to the Knott-Zoeppritz equations, proposed by Fatti et al. (1994), where AVO is estimated by fitting the amplitudes at a particular time to a linearized equation that describes the amplitude behaviour at each offset, usually with a least-squares fit. Fatti et al. have proposed the following linearized AVO equation as a model for  $S(\theta)$ :

$$S(\theta) \approx R_p \sec^2 \theta - 8 \frac{\beta^2}{\alpha^2} R_s \sin^2 \theta - \left( \frac{1}{2} \tan^2 \theta + 2 \frac{\beta^2}{\alpha^2} \sin^2 \theta \right) R_D, \quad (3)$$

where  $S(\theta)$  is the bandlimited reflectivity at any given incident angle  $\theta$ ,  $V_s/V_p$  is the background  $V_s/V_p$ , and where Fatti et al. have defined  $R_P$ ,  $R_S$ , and  $R_D$  as the P-wave, S-wave and density reflectivities, such that

$$R_P = \frac{1}{2} \left[ \frac{\Delta V_P}{V_P} + \frac{\Delta \rho}{\rho} \right] = \frac{1}{2} \frac{\Delta Z_P}{Z_P} \quad (4)$$

$$R_S = \frac{1}{2} \left[ \frac{\Delta V_S}{V_S} + \frac{\Delta \rho}{\rho} \right] = \frac{1}{2} \frac{\Delta Z_S}{Z_S} \quad (5)$$

$$R_D = \frac{\Delta \rho}{\rho}. \quad (6)$$

Linear inversion of equation 3 cannot recover estimates above or below the frequency range of the data and so we obtain bandlimited estimates of the reflectivities, denoted with “hats” as  $\hat{R}_P$ ,  $\hat{R}_S$  and  $\hat{R}_D$ , while  $R_P$ ,  $R_S$  and  $R_D$ , are the real-earth broadband reflectivities.. It should be noted that because of the limited offset distribution available for most seismic inversion experiments, the  $R_D$  term is often poorly constrained by the data and therefore either ignored or discarded for most experiments of this type.

The AVO inversion of prestack P-wave seismic gathers generates P-wave and S-wave reflectivity. As this example is inverting a synthetic dataset, building the background P- and S-Impedance for poststack inversion is a simple process of smoothing the well-log data used to generate the synthetic gathers. Using these background models, inversion of the reflectivity attributes to impedance attributes is possible through a poststack inversion of each reflectivity volume separately, following the outline provided by Hampson (1988). As discussed above, seismic reflection data is assumed to be a

bandlimited reflectivity sequence. This comes from the convolutional model of seismic data which states that

$$s(t) = r(t) * w(t) + n(t) \quad (7)$$

where  $s(t)$  is the seismic trace, which results from the convolution of a time series of reflectivity,  $r(t)$ , with a wavelet described by,  $w(t)$ , and added noise ( $n(t)$ ). However in this case, we have previously estimated reflectivities  $\hat{R}_p$  and  $\hat{R}_s$  by inverting equation (3), and these reflectivities are bandlimited as they were derived from bandlimited prestack seismic gathers. As a result, we recognize the relationship between real earth (broadband) reflectivity and the bandlimited reflectivity estimates which results via

$$\hat{R}_p(t) = R_p(t) * w_p(t) + n_p(t), \text{ and} \quad (8)$$

$$\hat{R}_s(t) = R_s(t) * w_s(t) + n_s(t) \quad (9)$$

where  $R_p$  and  $R_s$  refer to the real earth P-wave and S-wave reflectivities,  $w_p$  and  $w_s$  are the wavelets for the P and S seismic traces respectively.  $\hat{R}_p$  and  $\hat{R}_s$  are the bandlimited reflectivities resulting from the inversion of equation (3) from the P-wave CMP gathers ( $S(\theta)$ ). For the poststack inversion, reflectivity is defined as

$$R(t) = \lim_{\Delta t \rightarrow 0} \frac{Z(t + \Delta t) - Z(t)}{Z(t + \Delta t) + Z(t)} \quad (10)$$

where  $Z$  is either the P- or S-Impedance (depending upon which reflectivity),  $(t+\Delta t)$  refers to a point in the time series of reflectivity  $\Delta t$  after time  $t$ . Taking the limit, making the assumption that the impedance contrast across an interface is small such that

$$Z(t + dt) + Z(t) \approx 2Z(t), \quad (11)$$

and substituting the numerator of (10) with

$$\frac{Z(t+dt) - Z(t)}{t+dt-t} = \frac{dZ}{dt} \quad (12)$$

equation (10) can be rewritten such that

$$R(t) = \frac{Z(t+dt) - Z(t)}{Z(t+dt) + Z(t)} \approx \frac{1}{2} \frac{1}{Z} \frac{dZ}{dt} \quad (13)$$

and rearranging terms,

$$2R(t)dt = \frac{1}{Z} dZ \quad (14)$$

then integrating both sides of (12) yields

$$2 \int R(t)dt = \int \frac{1}{Z} dZ = \ln(Z) - \ln(Z_0) = \ln\left(\frac{Z}{Z_0}\right) \quad (15)$$

where  $-\ln(Z_0)$  is a constant of integration. Substituting the result from (15) into equations

(8) and (9) and defining

$$L(t) = \ln\left(\frac{Z(t)}{Z_0}\right) \quad (16)$$

yields

$$\hat{R}_p(t) = \frac{1}{2} \frac{d}{dt} (L_p(t))^* w_p(t) + n_p(t), \text{ and} \quad (17)$$

$$\hat{R}_s(t) = \frac{1}{2} \frac{d}{dt} (L_s(t))^* w_s(t) + n_s(t), \quad (18)$$

or in matrix notation

$$\hat{R}_p = \frac{1}{2} DL_p W_p + N_p, \text{ and} \quad (19)$$

$$\hat{R}_s = \frac{1}{2} DL_s W_s + N_s \quad (20)$$

where  $D$  is a derivative matrix,  $W_P$  and  $W_S$  are Toeplitz matrices formed from the wavelet for the P- and S-wave seismic traces respectively (Yilmaz, 2001).  $N_P$  and  $N_S$  are the matrices that represent noise on the P-wave and converted wave data respectively. Due to the bandlimited nature of seismic data, specifically the lack of low frequencies, an initial model reflecting the low frequency trend (e.g. 0 – 10 Hz) of the impedances is used as an initial solution in an iterative inversion in order to properly recover the impedance information from the seismic trace (Lindseth, 1979).

While not discussed in this work, in general it is possible for the noise to be different on each of  $R_P$  and  $R_S$ . This noise difference, can be accounted for either with additional processing on the reflectivity volumes, or by adjusting the prewhitening in the inversion, so as to better stabilize the solution. Additionally, while not mentioned in this work, the wavelet could change in both space and time or even between reflectivity volumes ( $\hat{R}_p$  and  $\hat{R}_s$ ), however the inversions presented here assume the wavelet is both non-changing (i.e. stationary), and consistent between  $\hat{R}_p$  and  $\hat{R}_s$  volumes for the purposes of the independent impedance inversions. In order to preserve continuity between the inverted volumes, consistent models and inversion parameters were applied for each inversion.

After the inversions for P- and S-Impedance have completed, the calculation of  $V_p/V_s$  is simple, i.e.

$$\frac{V_P}{V_S} = \frac{Z_p}{Z_s}. \quad (21)$$

The  $V_p/V_s$  resulting from AVO + prestack inversion of the synthetic gather is shown in figure 2.6.

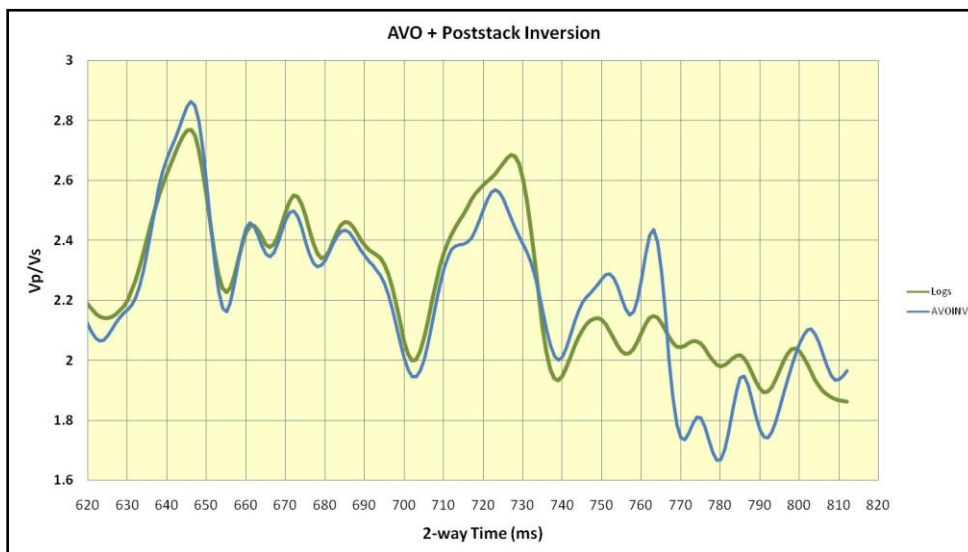


**Figure 2.6: Comparison of  $V_p/V_s$  from logs (green) and AVO + Poststack Inversion (blue). Zone of interest is between 750 and 770 ms. Note that the inverted trace shows good agreement with the log except between 760 – 795 ms, which includes the zone of interest.**

### 2.3 Prestack inversion with P-wave synthetic data

The procedure for prestack inversion of P-wave seismic data follows the workflow presented by Hampson et al. (2005). The intent with this workflow is to calculate the same attributes as the workflow presented above, with fewer steps, and in a more integrated fashion. One of the less favourable aspects of the poststack inversion method described above is that inversions for P-Impedance and S-Impedance, with the exception of the models, are independent of one another. Non-correlated noise can cause problems because the signal-to-noise ratio of the reflectivity volumes is often different and the resulting inversion can respond to this independently on each volume. By

performing the inversion prestack, we are able to solve for P-wave impedance and S-wave impedance simultaneously, thereby treating errors equally on both volumes.

The method proposed by Hampson et al. incorporates published rock physics relationships into the Fatti et al. equation discussed above. Castagna et al. (1985) have established an empirical relationship between P-wave and S-wave velocities from the Gulf of Mexico, of the form

$$V_s = xV_p + y \quad (22)$$

where  $x = 1.16$  and  $y = 1360$  m/s in the original publication, but could vary slightly due to local geology. While this equation is based upon measured rock properties from the Gulf of Mexico, it provides a good relationship to a variety of clastic rocks in a variety of basins. Similarly, Gardner has proposed an equation between P-wave velocity and density which is of the form

$$\rho = aV_p^b \quad (23)$$

where  $a = 0.23$  and  $b = 0.25$ , which was similarly derived for Gulf of Mexico clastics. Together, these two equations allow for a reformulation of the equation by Fatti et al. (1992) to solve for P-wave Impedance and the misfit to the model of general forms of both the Castagna et al. and Gardner et al. equations.

Using the same assumptions as made in the derivation of equations (11) to (15), equations (4) to (6) can be rewritten such that

$$R_p = \frac{1}{2} \left[ \frac{\Delta V_p}{V_p} + \frac{\Delta \rho}{\rho} \right] = \frac{1}{2} \frac{\Delta Z_p}{Z_p} \approx \frac{1}{2} \left[ \ln \left( \frac{Z_p}{Z_{p_0}} \right) \right] \quad (24)$$

$$R_s = \frac{1}{2} \left[ \frac{\Delta V_s}{V_s} + \frac{\Delta \rho}{\rho} \right] = \frac{1}{2} \frac{\Delta Z_s}{Z_s} \approx \frac{1}{2} \left[ \ln \left( \frac{Z_s}{Z_{s_0}} \right) \right] \quad (25)$$

$$R_D = \frac{\Delta \rho}{\rho} \approx \left[ \ln \left( \frac{Z_D}{Z_{D_0}} \right) \right]. \quad (26)$$

This allows a reformulation of equation (3) given by

$$S_\theta = \frac{1}{2} c_1 W_\theta D L_P + \frac{1}{2} c_2 W_\theta D L_S + c_3 W_\theta D L_D \quad (27)$$

where  $L_P$ ,  $L_S$  and  $L_D$  are defined as the natural logarithm of P-Impedance, S-Impedance and density respectively,  $W_\theta$  is the wavelet matrix at each angle  $\theta$ , and

$$c_1 = 1 + \tan^2 \theta = \sec^2 \theta \quad (28)$$

$$c_2 = -8 \frac{V_S^2}{V_P^2} \tan^2 \theta \quad (29)$$

$$c_3 = -\frac{1}{2} \tan^2 \theta + 2 \frac{V_S^2}{V_P^2} \sin^2 \theta. \quad (30)$$

However, due to the relationships described in (22) and (23),  $L_S$  and  $L_D$  can be formulated in terms of  $L_P$ , adding a constraint to the solution, such that

$$L_S = k L_P + k_C + \Delta L_S \quad (31)$$

and

$$L_D = m L_P + m_C + \Delta L_D \quad (32)$$

By incorporating equations (34) and (35), equation (30) can now be written as

$$S_\theta = C_1 W_\theta D L_P + \frac{1}{2} c_2 W_\theta D \Delta L_S + c_3 W_\theta D \Delta L_D \quad (33)$$

or in matrix form with  $M$  angle traces as

$$\begin{bmatrix} S_{\theta_1} \\ \dots \\ S_{\theta_M} \end{bmatrix} = \begin{bmatrix} C_1 W_{\theta_1} D & \frac{1}{2} c_2 W_{\theta_1} D & c_3 W_{\theta_1} D \\ \dots & \dots & \dots \\ C_1 W_{\theta_M} D & \frac{1}{2} c_2 W_{\theta_M} D & c_3 W_{\theta_M} D \end{bmatrix} \begin{bmatrix} L_P \\ \Delta L_S \\ \Delta L_D \end{bmatrix} \quad (34)$$

where

$$C_1 = \frac{1}{2} c_1 + \frac{1}{2} k c_2 + m c_3. \quad (35)$$

Similar to the poststack inversion above, the low frequencies are missing from the seismic data and cannot be recovered from the inversion without additional input. The method implemented by Hampson et al. sets a low frequency background model for P-Impedance, which indirectly also sets the background model for the S-Impedance and density by the relationships defined in equations (31) and (32), which then iterates to a solution. For the purpose of the initial model,  $\Delta L_S$  and  $\Delta L_D$  are set to zero and iteratively solved through the inversion along with  $L_P$ . There are a variety of mathematical tools available to solve this inversion, including L-1 or L-2 norms, singular value decomposition (Aster et al., 2005), however Hampson et al. have implemented their algorithm with a conjugate gradient algorithm in order to maintain numerical stability and computational efficiency.

In the case of the synthetic gather, the same impedance models used for the poststack inversions were again used for the prestack inversion, so as to test the algorithm and not the models used. Since we generated the input wavelet ourselves, we can select that same wavelet for the inversion. This, however, will not account properly for NMO-stretch on the gather (Downton, 2005), though in using angles less than 30 degrees, NMO-stretch has been assumed to be negligible. The input to the prestack inversion is the synthetic angle gather previously discussed. By performing the prestack inversion,

we reduce two inversion processes to a single inversion, and better link the inversion solutions as both the P- and S-Impedance volumes are solved simultaneously, thereby minimizing the solution error on both attributes at the same time. The limitation, however, is that the traces being inverted generally have lower signal-to-noise ratios as compared to stacked data, raising the possibility that the inversion could be more susceptible to noise on real gathers, however this is partially mitigated by utilizing partially-stacked angle gathers (e.g. 35-fold offset gather converted to 5-fold angle gather). Additionally, by utilizing multiple angles at each CMP location, the noise attenuation benefit of stacking indirectly results, providing further stabilization to the solution. Figure 2.7 shows the resulting  $V_p/V_s$  from the prestack inversion.

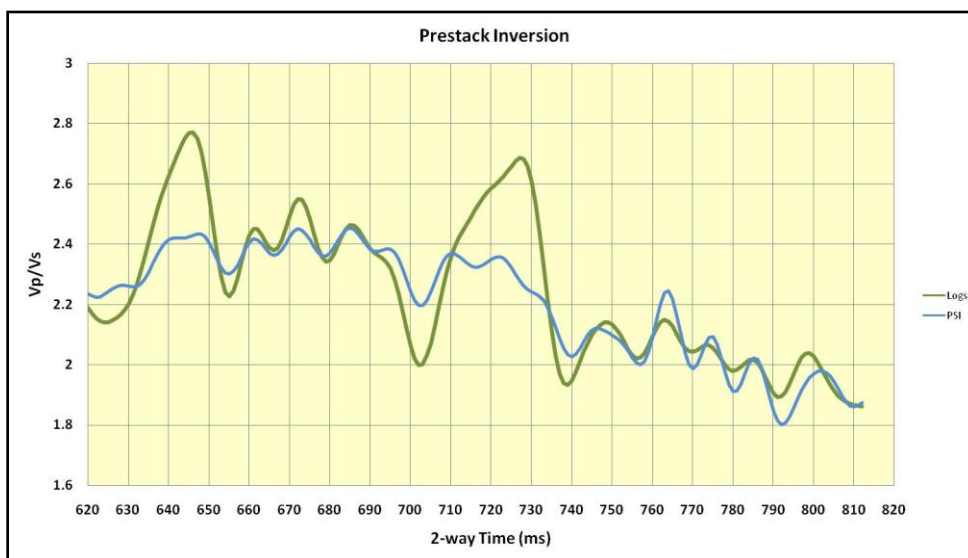


**Figure 2.7: Comparison of  $V_p/V_s$  from logs (green) and prestack inversion (blue). Zone of interest is between 750 and 770 ms. Note the improved correlation to the log over the zone of interest as compared to figure 2.6.**

## 2.4 Prestack inversion with P-wave and converted-wave synthetic data

Integration of the converted-wave data to the inversion follows a similar path as previously defined for the PP-only prestack inversion. Using the same P-wave angle gathers created for the previous inversion, we also include input from the converted-wave data. As in the previous inversion, the PP angle gathers are loaded into the inversion, however this time the converted wave gathers are also included. While still only requiring a single inversion step, it is hoped that the addition of converted wave data will improve the Vp/Vs estimate by providing an additional “independent” response of the seismic data, which must fit the same resulting inversion result.

The inversion method is extended to include PS data by utilizing a formulation of the PS-AVO equation as published by Stewart (1990), where

$$R_{PS} = \frac{-\alpha \tan \phi}{\beta} \left( 4 \sin^2 \phi - 4 \frac{\beta}{\alpha} \cos \theta \cos \phi \right) R_S + \frac{\alpha \tan \phi}{2\beta} \left( 1 + 2 \sin^2 \phi - 2 \frac{\beta}{\alpha} \cos \theta \cos \phi \right) R_D \quad (36)$$

By including these additional terms in the inversion discussed in the previous method, the solution of P-Impedance, S-Impedance and density are optimized for both the PP- and PS-data.

Incorporating this additional data into the prestack inversion discussed above simply requires adding two additional inputs into equation (34), such that;

$$\begin{bmatrix} S_{PP\theta_1} \\ \vdots \\ S_{PP\theta_N} \\ S_{PS\theta_1} \\ \vdots \\ S_{PS\theta_M} \end{bmatrix} = \begin{bmatrix} A_{PP\theta_1} W_{PP\theta_1} D & \frac{c_2}{2} W_{PP\theta_1} D & c_3 W_{PP\theta_1} D \\ \vdots & \vdots & \vdots \\ A_{PP\theta_N} W_{PP\theta_N} D & \frac{c_2}{2} W_{PP\theta_N} D & c_3 W_{PP\theta_N} D \\ B_{PS\theta_1} W_{PS\theta_1} & B_{PS\theta_1} W_{PS\theta_1} & C_{PS\theta_1} W_{PS\theta_1} \\ \vdots & \vdots & \vdots \\ B_{PS\theta_M} W_{PS\theta_M} & B_{PS\theta_M} W_{PS\theta_M} & C_{PS\theta_M} W_{PS\theta_M} \end{bmatrix} \begin{bmatrix} L_P \\ \Delta L_S \\ \Delta L_D \end{bmatrix} \quad (37)$$

where;

M represents the number of PS angle traces,

$$A_{\theta} = \frac{1}{2}c_1 + \frac{1}{2}kc_2 + mc_3, \quad (38)$$

$$B_{\theta,\phi} = \frac{V_P}{V_S} \tan \phi_1 \left[ 4 \sin^2 \phi_1 - 4 \frac{V_S}{V_P} \cos \theta_1 \cos \phi_1 \right], \quad (39)$$

$$C_{\theta,\phi} = -\frac{V_P}{2V_S} \tan \phi_1 \left[ 1 + 2 \sin^2 \phi_1 - 2 \frac{V_S}{V_P} \cos \theta_1 \cos \phi_1 \right], \quad (40)$$

$$\phi = \sin^{-1} \left( \frac{V_S}{V_P} \sin \theta \right). \quad (41)$$

In the case of the synthetic example, two methods are used to register the PS-gather to PP-time for the inversion. The first is to use the  $V_p/V_s$  of the log data, which is the exact solution for the synthetic model generated for this experiment, though this is unknown for conventionally processed multicomponent seismic data. The joint prestack inversion results of the model are shown in figure 2.8.

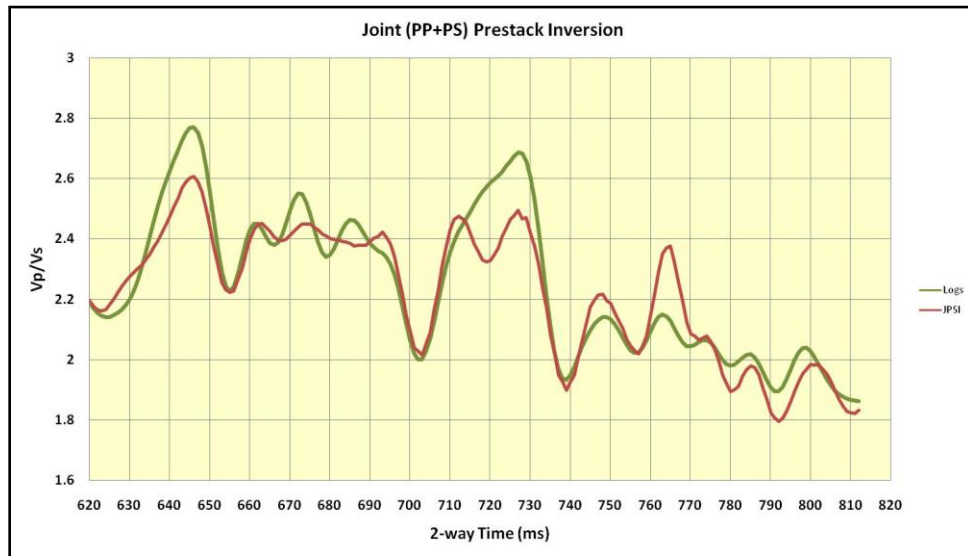


**Figure 2.8: Comparison of Vp/Vs from logs (green) and Joint Prestack Inversion (red). Zone of interest is between 750 and 770 ms. Note the improvement in the correlation to the log trace over the entire trace interval displayed including the zone of interest.**

## 2.2 Discussion – inversions of synthetic data

In order to better understand and compare the results from the above inversions, the Vp/Vs from each inversion is compared to a band-limited Vp/Vs calculated from well logs. Starting with a comparison of the correlation between the inversion result and the log data (Figure 2.9), we can see that over the inverted window, the correlation is quite high in all cases (above 85%), however, when focusing into the zone of interest, important differences begin to emerge which dramatically change the correlation coefficient. Figure 2.10 shows the inversion results compared to the filtered log data for comparison.

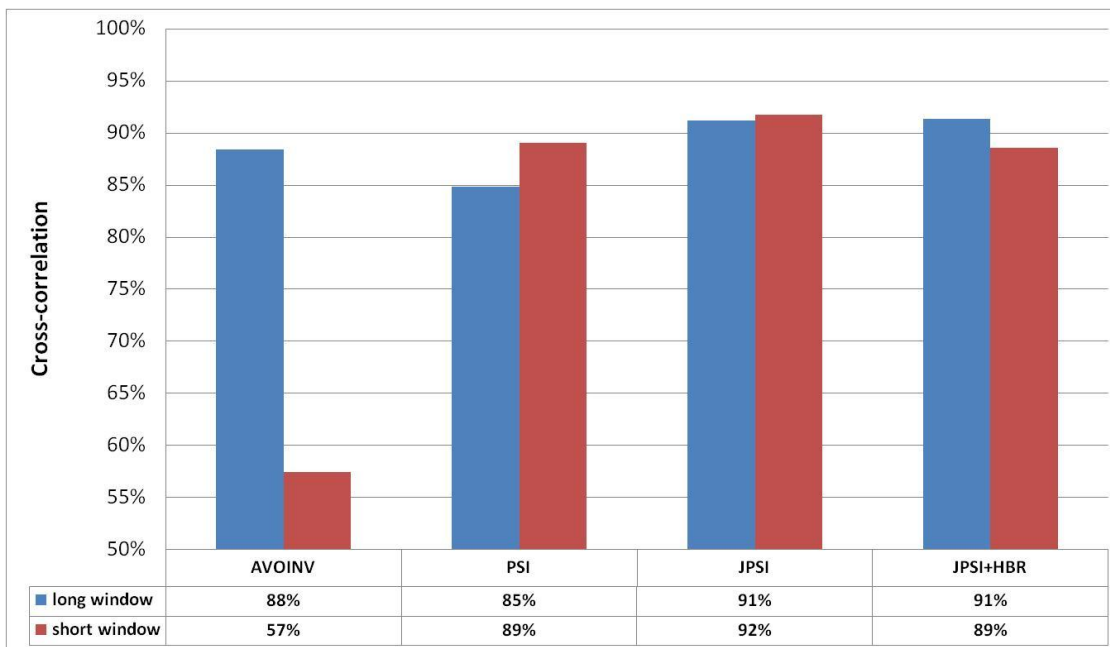


**Figure 2.9: Correlations between Vp/Vs from well logs with estimates from the various inversion methods with both long (312 ms) and short (73 ms) correlation windows around the zone of interest. All prestack inversion methods (PSI, JPSI, JPSI+HBR) appear to be significantly better in the zone of interest (short window).**

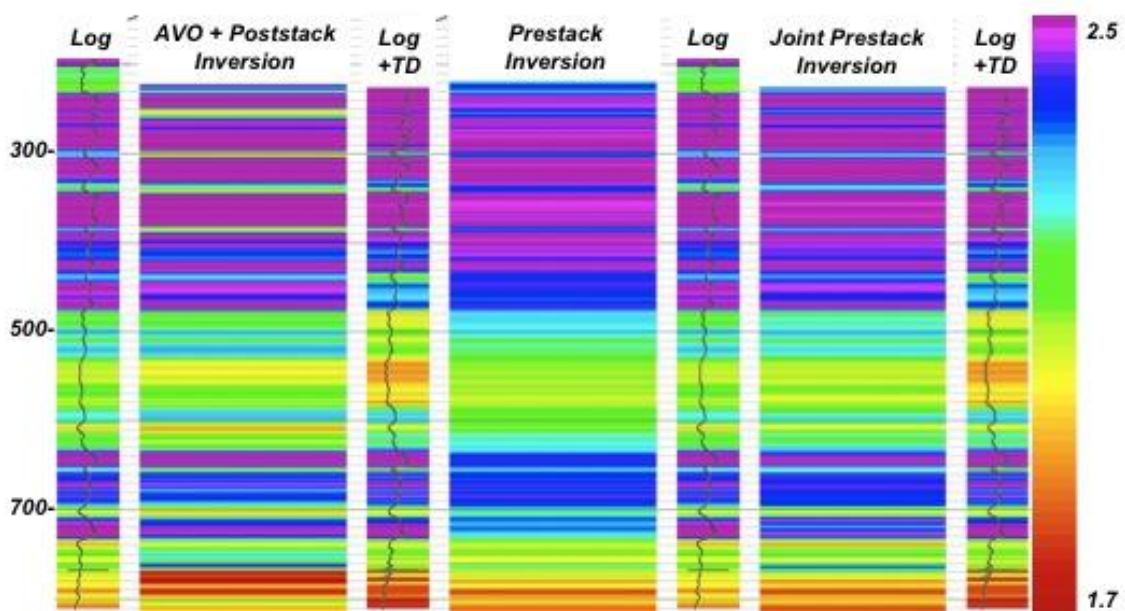


**Figure 2.10: Comparison of the three inversion methods against well control. Track 1 shows the  $V_p/V_s$  from well log data, track 2 shows  $V_p/V_s$  from AVO + poststack inversion of the model gather. Track 3 shows the  $V_p/V_s$  of the well logs which have been corrected by the time-depth relationship derived from correlation with both the PP and PS seismic data. Track 4 is the  $V_p/V_s$  ratio from prestack inversion and track 5 is a duplicate of track 1. Track 6 shows the  $V_p/V_s$  from the joint prestack inversion, while track 7 is a duplicate of track 3.**

In the case of AVO + poststack inversion, the correlation coefficient for the  $V_p/V_s$  decreases from 88% using a window length of 312 ms, to 52% when examining a shorter window around the zone of interest (figure 6.1). When examining the output of the other three inversions performed, the difference in correlation coefficients between long and short windows is not as dramatic, with correlations ranging from 85% to 92%. Because the correlation over the long window for the AVO + poststack inversion is 88%, it appears that the inverted result is a close representation to the real  $V_p/V_s$ . However when examining this result over the short window which is more directly focused immediately around the zone of interest. The coals which surround the zone of interest

exhibit very high reflectivities, which is a violation of the small-reflectivity assumption (i.e.  $R(\theta) \ll 1$ ) built into most linearized-AVO methods (Aki and Richards, 1980). It appears the high reflectivity has introduced an error into the AVO and subsequent inversion results, introducing an error in the output inversion result through the zone of interest.

Prestack inversion has significantly improved the result through the zone of interest, as compared to the previous method, with the correlation at the zone of interest at 89%, however the correlation of the longer window appears to have been compromised by the mismatch to the wells shallower in the section. Interestingly, the prestack inversion algorithm used is also based upon the Aki and Richards equations, and so should be compromised by the high reflectivities at the coals, similar to the AVO example above, though this does not appear to be the case when comparing the results of the inversion to well control.

As expected, joint prestack inversion has slightly improved the inversion result in this noise-free synthetic example, with correlations of 91% and 92% for the long and short windows respectively. In general, the shallower zones at 636-650 ms and 712-734 ms exhibit a better match to well control over the prestack inversion without PS-data and the match at the zone of interest is almost identical to the previous result (Figure 2.11), though there are some changes at the coals where the joint prestack inversion has been slightly degraded. This degradation near the coals could be due to wavelet changes not accounted for when changing domains from PP-time to PS-time.

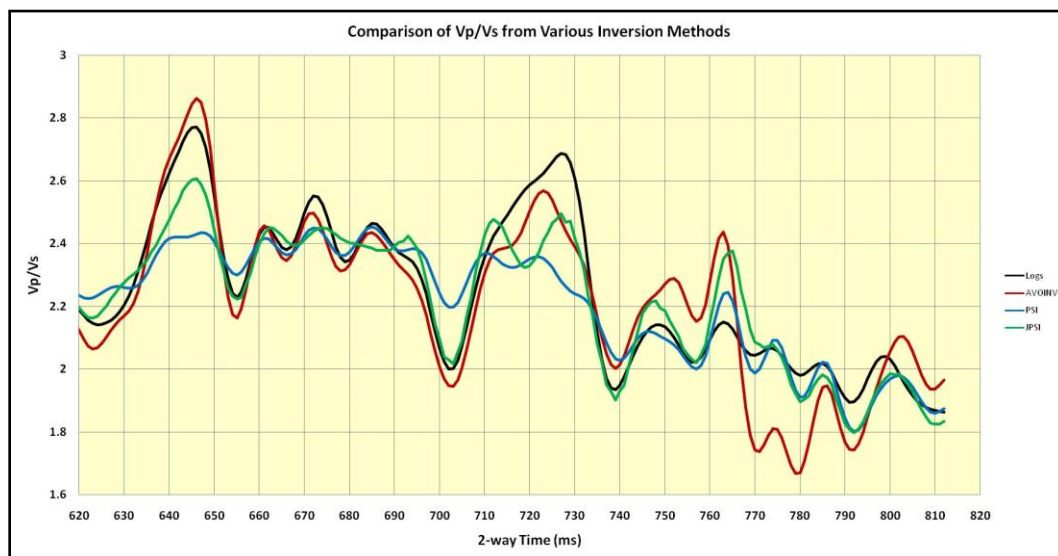


**Figure 2.11: Well log Vp/Vs (black) compared to the AVO + poststack inversion (red), prestack inversion (blue), and joint prestack inversion (green). Note that all prestack inversion methods correlate better over the zone of interest (740 ms – 780 ms) than the AVO + poststack inversion technique.**

A second method for correlating PP- and PS-data to a common domain utilizes horizons picked independently on the P-wave and converted wave volumes which are intended to be geologically identical and are forced to match, as described in a later section, which results in a Vp/Vs. Due to frequency content and phase differences between the PP and PS volumes, even on synthetic data, small errors in Vp/Vs estimates can occur with horizon-based registration. These small errors can have an impact upon the inversion results that follow by introducing errors. To test the impact of small errors from manual registration, the horizons used for the seismic data registration are the same horizons used for the registration test on the synthetic data. A comparison of Vp/Vs from logs and from registration of the synthetic data is shown in figure 2.12.

As discussed above, PS-data is compressed to PP-time, which has the effect of distorting the wavelet in a time-variant sense. Because the amount of compression is proportional to the  $V_p/V_s$  ratio in the interval, this effectively creates a time-variant wavelet on the PS-data that has not been accounted for in the inversion process and could be the source of the degraded inversion result at this level.

As mentioned above, the  $V_p/V_s$  to be used for registration is generally not known everywhere, even with monopole or dipole shear sonic logs (though they can be used at well locations). Therefore  $V_p/V_s$  must be approximated, often by correlating horizons between PP- and PS-volumes. Due to frequency content and reflectivity differences between these volumes, accurately registering events on a sample-by-sample basis is a formidable task. This can introduce errors in the inversion, but what impact does this have on the inversion result? The joint prestack inversion was repeated using horizon-based registration identical to that used for the real seismic data in the sections that follow. In comparing the results in detail, a small error has been introduced, which, when considering the process of registering PS-data to PP-time, appears to have manifested as a delay (figure 2.12). Some samples appear to be perfectly aligned as compared to the result using the correct  $V_p/V_s$ , others appear to exhibit a delay of 1-2 samples. Additionally, amplitudes have also been changed slightly as compared to the previous inversion result. This indicates that even small registration errors (i.e. on the order of one sample) are sufficient to degrade the results from joint prestack inversion.

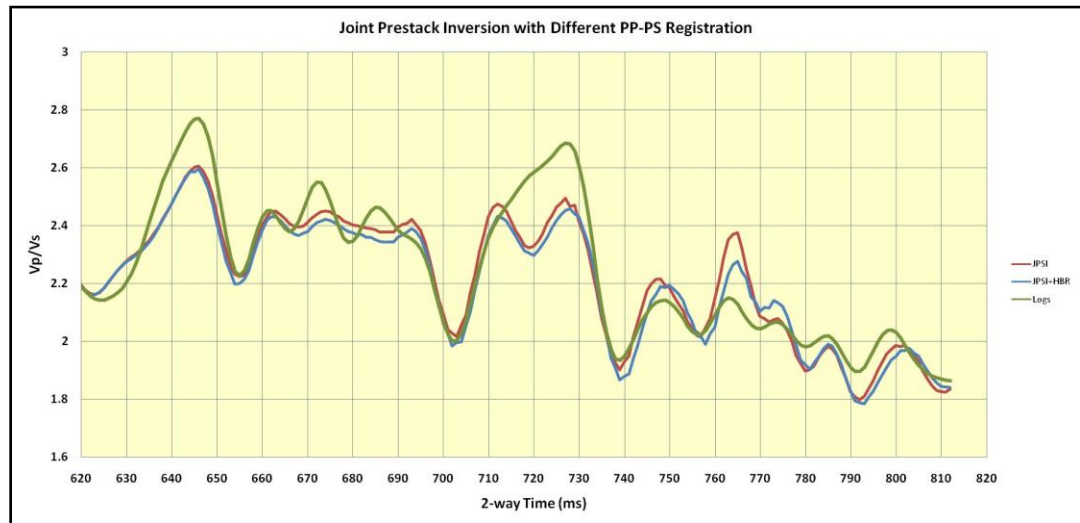


**Figure 2.12: Comparison of Joint Prestack Inversion results using different registration methods. Green = logs, Red = Joint Prestack Inversion (JPSI), Blue = Joint Prestack Inversion with Horizon Based Registration (JPSI+HBR). Results are in good agreement above the zone of interest, however amplitude and/or phase distortions are apparent within the zone of interest (740 – 780 ms). Registration time difference is approximately 1 ms (1 sample).**

### Chapter Three: Inversions comparisons of real seismic data

#### 3.1 AVO + poststack inversion method on P-wave seismic data

The gathers, as delivered by the processor, have additional processing applied in order to help improve the solutions. This consisted of a mute function applied to the data, as well as a 3x3 superbin, in order to improve the signal-to-noise ratio at each offset through partial stacking (Ostrander, 1984). A maximum angle of 30° was used for the AVO inversion, as larger angles begin to exhibit problems with normal moveout removal, either from inappropriate velocities, or non-hyperbolic moveout. AVO inversion used a background relationship between shear-wave velocity and P-wave velocity given by the mud-rock line (Castagna, 1984),

$$V_s = -1172 + 0.862 * V_p. \quad (42)$$

Figure 3.1 shows an example of a characteristic offset gather with angles defined as the background colour. In following the workflow described by Goodway et al. (1997), P-wave and S-wave reflectivities are first estimated (figure 3.2).

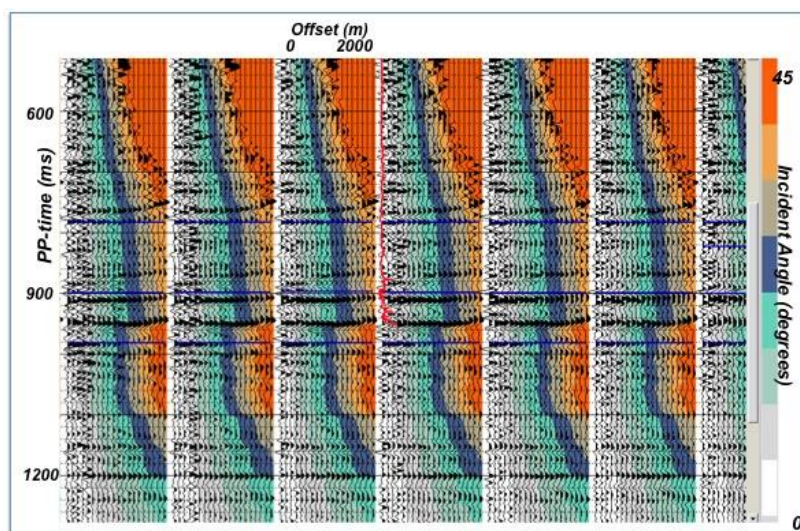


**Figure 3.1: Prestack P-wave seismic data. Angles are displayed as colour background. Target zone has a maximum angle slightly above 30°**

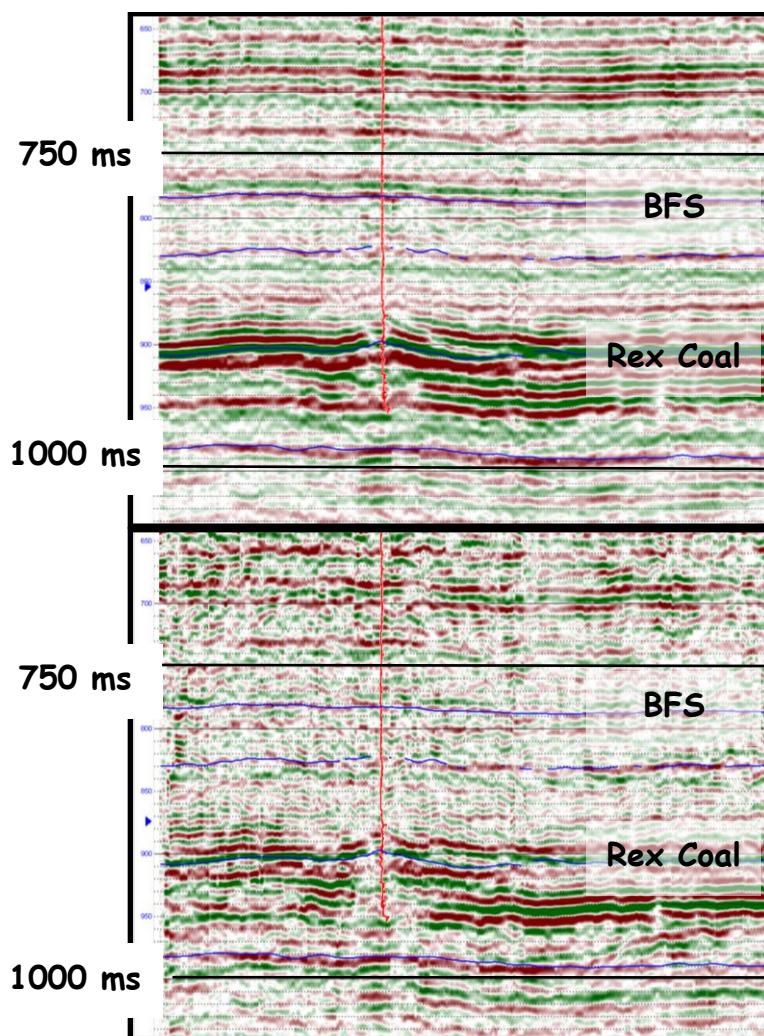


**Figure 3.2: AVO attributes  $R_P$  (top) and  $R_S$  (bottom). For location reference, the sonic log from Well F is shown as the red trace in the displays. Key horizons are identified by blue lines. The zone of interest is at approximately 925 ms, immediately below the “Rex Coal” horizon. The lateral extent of the section displayed is approximately 4.1 km (2.57 miles) long.**

A single well log was used to build the impedance models. This well (Well E) contained measured conventional and shear sonic logs, in addition to density and other commonly acquired well log data. We therefore have a direct measurement of the velocities for both P-waves and S-waves, in the vicinity of the borehole. Using the sonic logs available from four wells, time-depth relationships were created by manually

aligning key events. A synthetic trace was created using the reflectivity derived from the sonic and density logs, convolved with a zero-phase wavelet extracted (Hampson, 1988) from the seismic data (Figure 3.3). The quality of the well log correlations was quite good, as shown in Figure 3.4. An independent wavelet (zero-phase statistical) was used in the inversion of the S-wave volume. This was done to better reflect the amplitude spectrum present on the S-wave reflectivity volume.

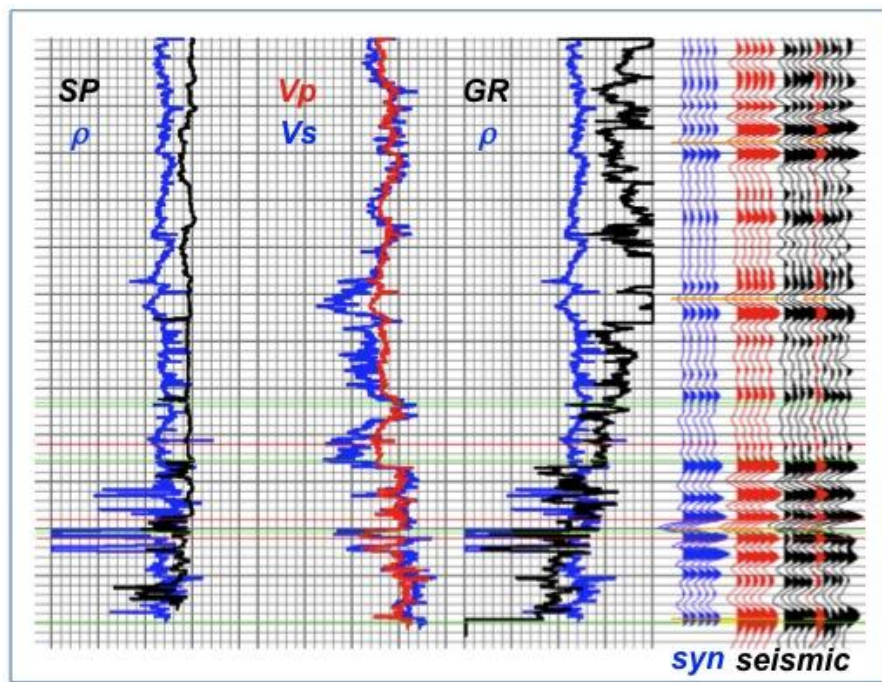


**Figure 3.3: P-wave synthetic to seismic well tie for well D. The blue wiggle trace is the synthetic and the red wiggle trace is the seismic data at the well location. Correlation is 69%.**

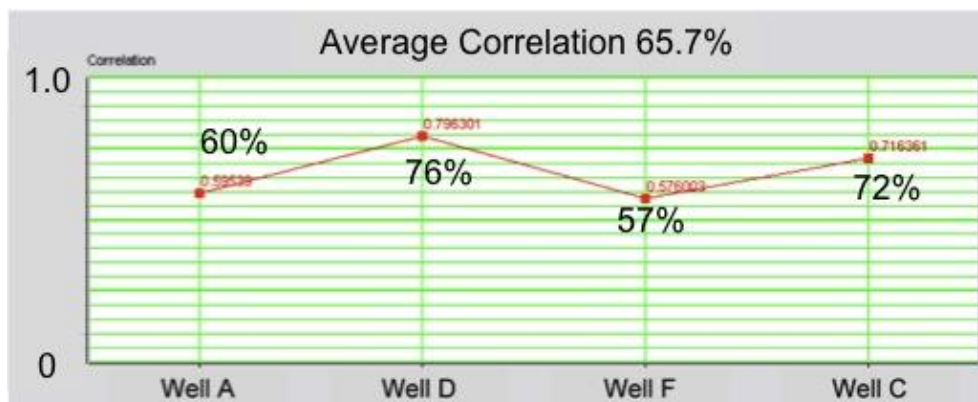


**Figure 3.4: P-wave synthetic correlations to seismic data at four wells, indicating reasonable quality well ties.**

Using the time-depth relationship for Well A, an impedance model was created to be used for the P-wave and S-wave inversions. In the case of the poststack inversion of the AVO attributes, a model-based inversion was performed. The inversion parameters are specified in Table 1, and are consistent for both the P-wave and S-wave inversions.

Prewhitening		1%
Scalar Adjustment Factor		1
Number of Iterations		10
Maximum Impedance Change		$\pm 100\%$
Average Block Size		2 ms
Scaling Window	Top	200 ms above Base Fish Scales
	Base	50 ms below Rex Coal

**Table 1: Poststack inversion parameters**

Figure 3.5 is an example of the calculated  $V_p/V_s$  volume. The correlation of the  $V_p/V_s$  volume from poststack inversion to well control will be discussed later.

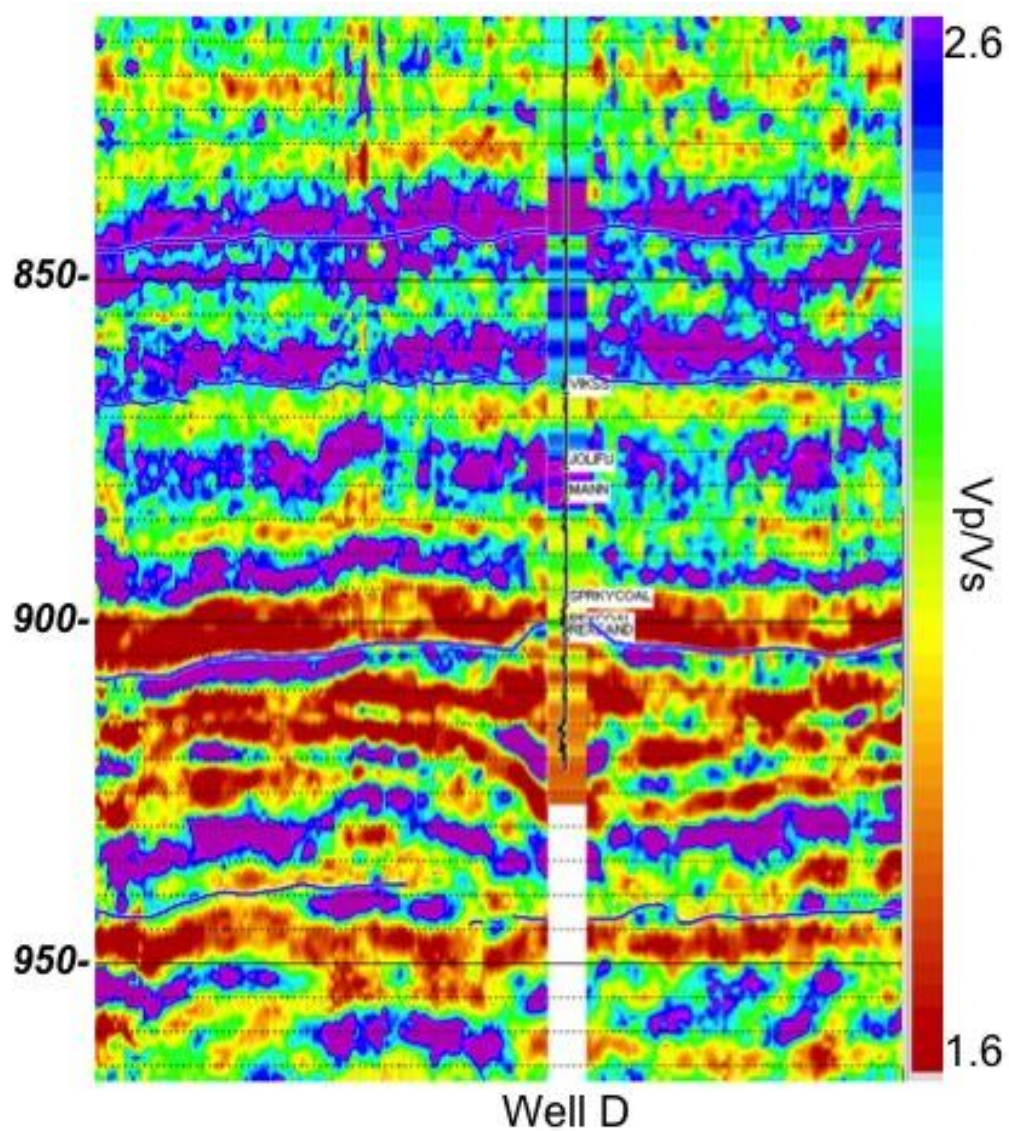
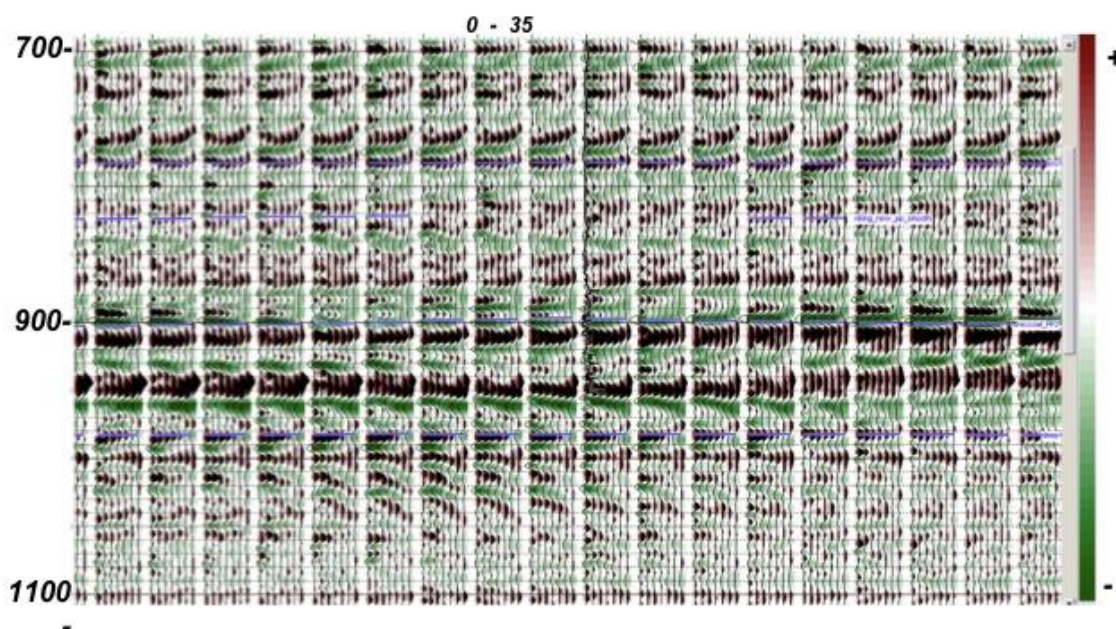


Figure 3.5: Vp/Vs from AVO + poststack inversion. Vp/Vs from logs at Well D has been inserted in color and the SP log as the trace.

### 3.2 Prestack inversion with P-wave seismic data

The same gathers used for the AVO extraction were used as a starting point for the prestack inversion. Using the stacking velocities, the offset gathers were converted to angle gathers (Figure 3.6), using seven angles between  $0^\circ$  and  $35^\circ$ . For the inversion, however, only angles between  $5^\circ$  and  $30^\circ$  were used, due to acquisition footprint issues (near offsets) and NMO-correction errors (far offsets).



**Figure 3.6: 7-fold ( $0^\circ$ - $35^\circ$ ) angle gathers from around Well F.**

In order to maintain consistency, the background model used for the poststack inversions was also used for the prestack inversion. Because the algorithm is somewhat different, parameterization is not the same between the poststack and prestack inversions. This difference originates from the prestack inversion optimizing the solution using seven prestack traces at each CMP location, instead of one poststack trace. In building the background model used for the prestack inversion, trends between P-impedance, S-

impedance and density are required. The inversion then iteratively determines an angle-dependant reflectivity model that minimizes the error on the angle gathers as deviations from the input model (Hampson et al., 2005). These deviations from the model are then added back to the model and the process is repeated, generally with significantly more iterations than typically done with a poststack inversion to reach what is hoped to be a global minimum. Using the model built from Well A and the background relationships between P-Impedance, S-Impedance, and Density from four wells (Wells A, C, D and E), the prestack inversion parameters used are defined in Table 2 guided by the cross-plots shown in Figure 3.7.

Angles Used		5 – 35
Number of Iterations		50
Joint k (from Figure 3.7)		1.050752
Joint $k_c$ (from Figure 3.7)		-5.30515
Joint m (from Figure 3.7)		0.025122
Joint $m_c$ (from Figure 3.7)		-0.934635
Prewhitening	P-Impedance	25%
	S-Impedance	25%
	Density	100%
Scalar Adjustment Factor		1
Scaling Window	Top	75 ms above Base Fish Scales
	Base	50 ms below Rex Coal

**Table 2: Prestack inversion parameters. The terms “ $k_c$ ”, “k”, “ $m_c$ ” and “m” refer to the slope and intercept of the best fit lines for the cross-plots shown in Figure 8.2.**

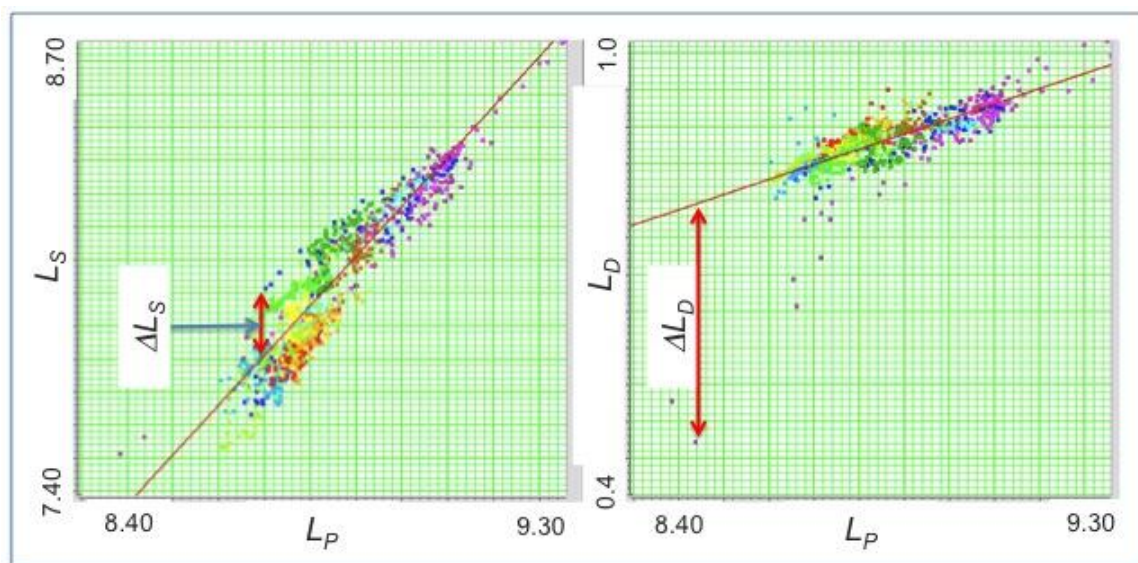


**Figure 3.7: Well log cross-plots to establish relationships ( $L_P$  vs.  $L_S$  and  $L_P$  vs.  $L_D$ ) for the background model. The left image is a cross-plot of the natural log of P-Impedance versus the natural log of S-Impedance. The right image is a similar plot of the natural log of P-Impedance versus the natural log of density. The geologic interval covers from the Second White Speckled Shale to the top of the coal sequence. Deviations along the vertical axis from the regression lines (red line) correspond to the  $\Delta L_S$  and  $\Delta L_D$  in equations X and X respectively. Large deviations may be indicative of a lithology change.**

In order to account for frequency content differences from near to far angles, near angle ( $5^\circ$ ) and far angle ( $25^\circ$ ) wavelets were extracted using the same parameters as the wavelets derived from the poststack inversion. This allows the wavelet to account for frequency dependant changes in the angle gathers that are not attributable to geology (frequency decay with offset, wavelet stretch from normal moveout removal – Figure 3.8, etc.). The resulting wavelets are shown in Figure 3.9. In this case, a full-phase wavelet was extracted using the method proposed by White (1997) to account for frequency dependant phase variations that are present in this data as the difference in the “average phase” (i.e. the intercept of a line fit through the phase versus frequency over the signal

band of the wavelet) is  $28^\circ$ . A profile from the resulting  $V_p/V_s$  volume is shown in Figure 3.10. Inserting the  $V_p/V_s$  log from the wells, the correlation is quite good over the zone of interest, again with the possible exception of the coal layers immediately above the target sand. This may be because the geology present here violates the small reflectivity assumption inherent in any method based upon the Aki and Richards (1980) equations.

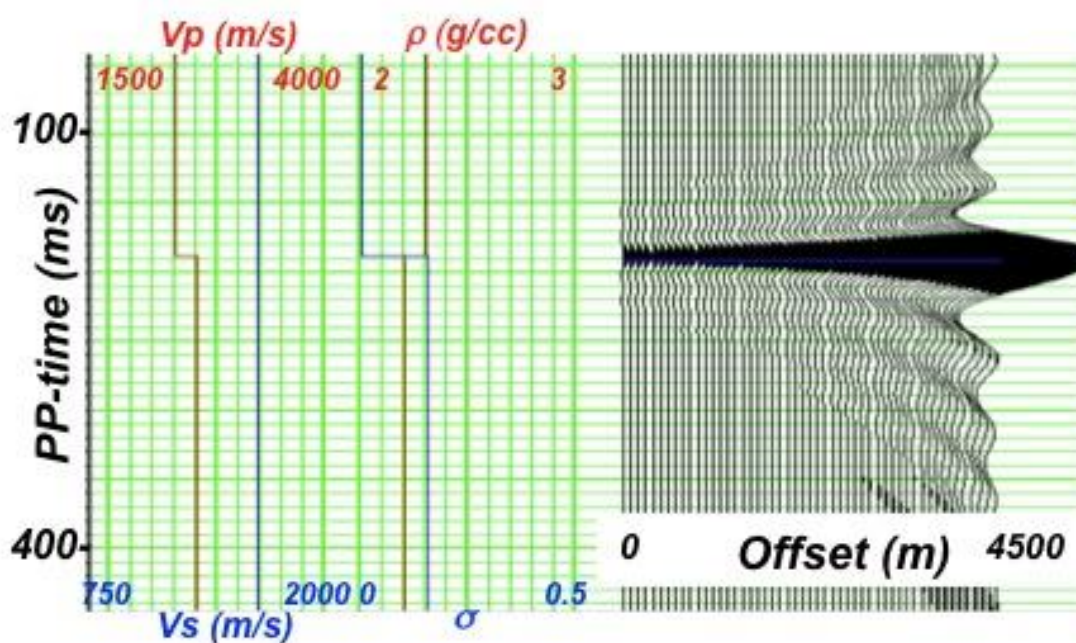


**Figure 3.8: Simple 1-layer model showing the exaggerated effect of NMO-stretch on a simple reflector. Note that the same wavelet was used to generate the synthetic at all offsets before normal moveout removal.**

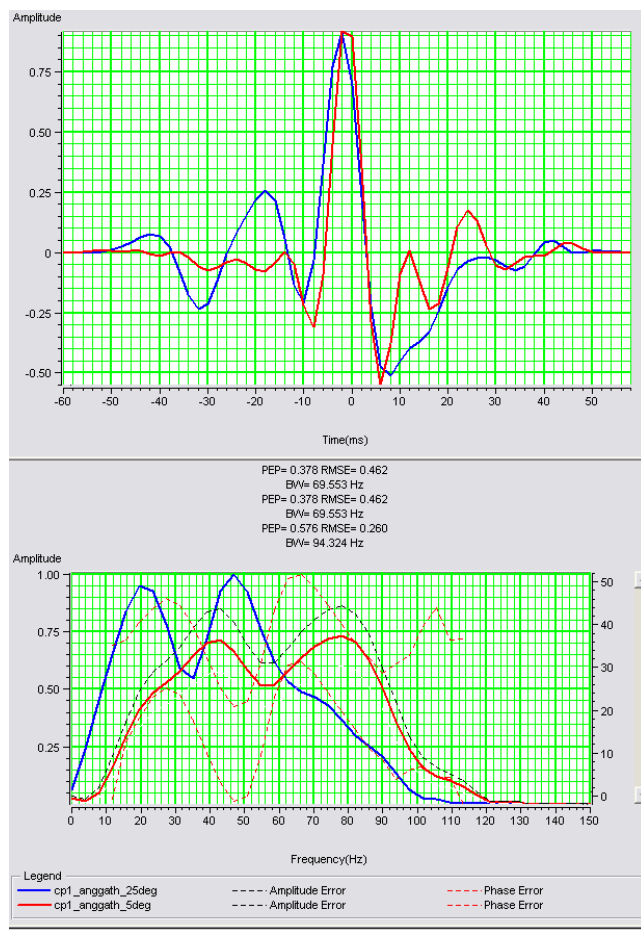


**Figure 3.9: Near (blue) and far (red) angle wavelets used in prestack inversion. In addition to differing frequency content, the average phase of the wavelet is  $26^\circ$  for the near angle and  $54^\circ$  for the far angle.**

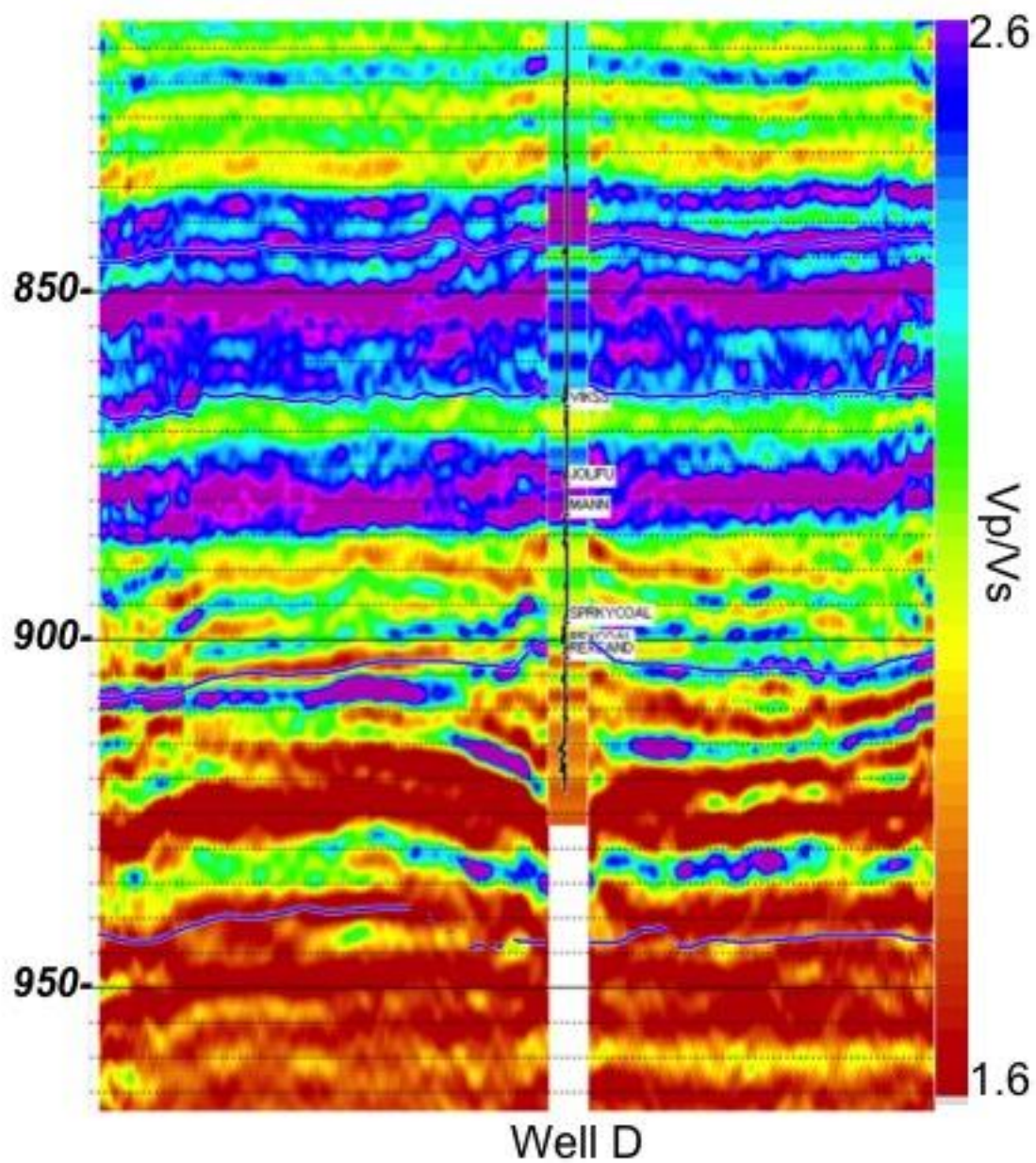
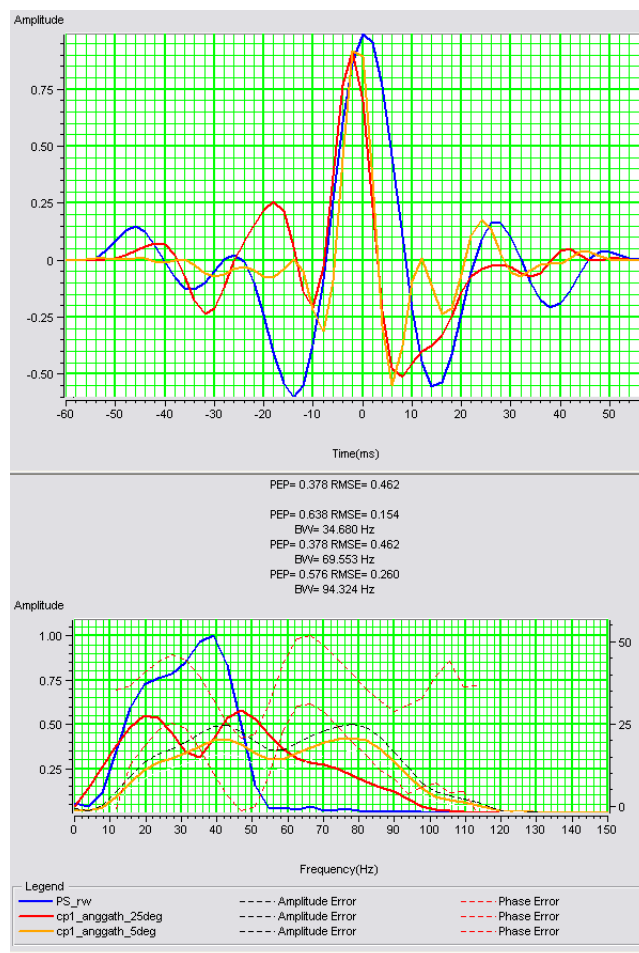


Figure 3.10:  $V_p/V_s$  from prestack inversion.  $V_p/V_s$  from logs at Well D has been inserted in color and the SP log as the trace.

### 3.3 Prestack inversion with P-wave and converted-wave seismic data

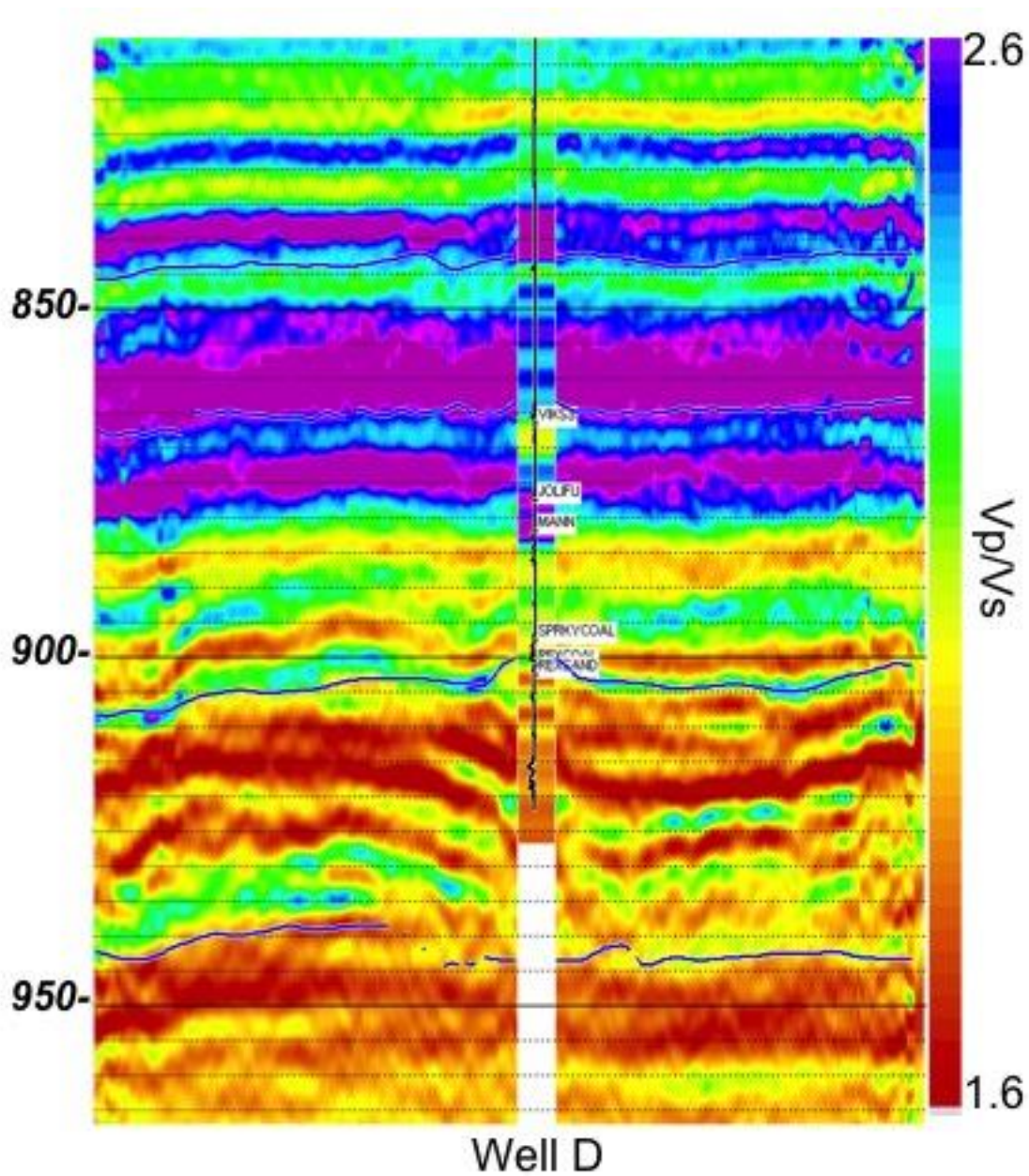
Now that we have the necessary information to register the converted-wave data to P-wave time, we can build the background model. This background model is the same as the model built in the previous prestack inversion, however it also incorporates the  $V_p/V_s$  from registration so as to register the converted-wave data as part of the inversion process. Wavelets also need to be defined for use in the inversion and for the P-wave data, we are again using the near- and far-angle wavelets extracted previously. It is now also necessary to derive a wavelet from the converted-wave data. This wavelet is derived from the converted-wave data in P-wave time over the same geologic intervals used for the P-wave wavelets. We can see in Figure 3.11 that the frequency content of the converted-wave data, even after compressing the time scale to P-wave time, remains significantly lower than that of the P-wave wavelets. Because the wavelets in the inversion program are defined at specific angles, but we are using a full-offset stack for the converted-wave data, we must choose an angle at which to define the converted-wave data and the corresponding wavelet. In this case we chose an angle of  $15^\circ$ , because low angles produce low converted-wave reflectivities (converted-wave reflectivity at zero-offset in an isotropic medium is zero), and the far offsets are muted, the dominant portion of the data will follow a corridor through the prestack gather and the volume will have an average angle close to  $15^\circ$ , analogous to weighted stacking for AVO analysis (Fatti, 1995; Smith and Gidlow, 1987; Stewart 1990). Small errors in the estimation of this angle can be accounted for in the inversion itself when calculating the scalar to apply to the converted-wave data, provided that the dominant angle of the converted-wave data does not change with respect to time (Stewart, 1990).



**Figure 3.11: Near (blue) and far (red) angle wavelets from P-wave data compared to the converted-wave wavelet used in joint prestack inversion. Note that the converted-wave wavelet is significantly lower bandwidth than either P-wave wavelet. The average phase on the converted-wave wavelet is  $-7^\circ$ .**

The inversion parameters are then selected and the inversion is performed. Because the P-wave data consists of multiple traces, but the converted-wave data is one trace, the inversion is biased towards the P-wave data, unless the converted-wave data is weighted higher (Hirsche, personal communication, 2003-2008). As such, inversions were tested with weights of 1.0 and 2.0, with a final selection of a weight of 1.0 being used for the full inversion as it appeared to suffer the least from the low-frequency

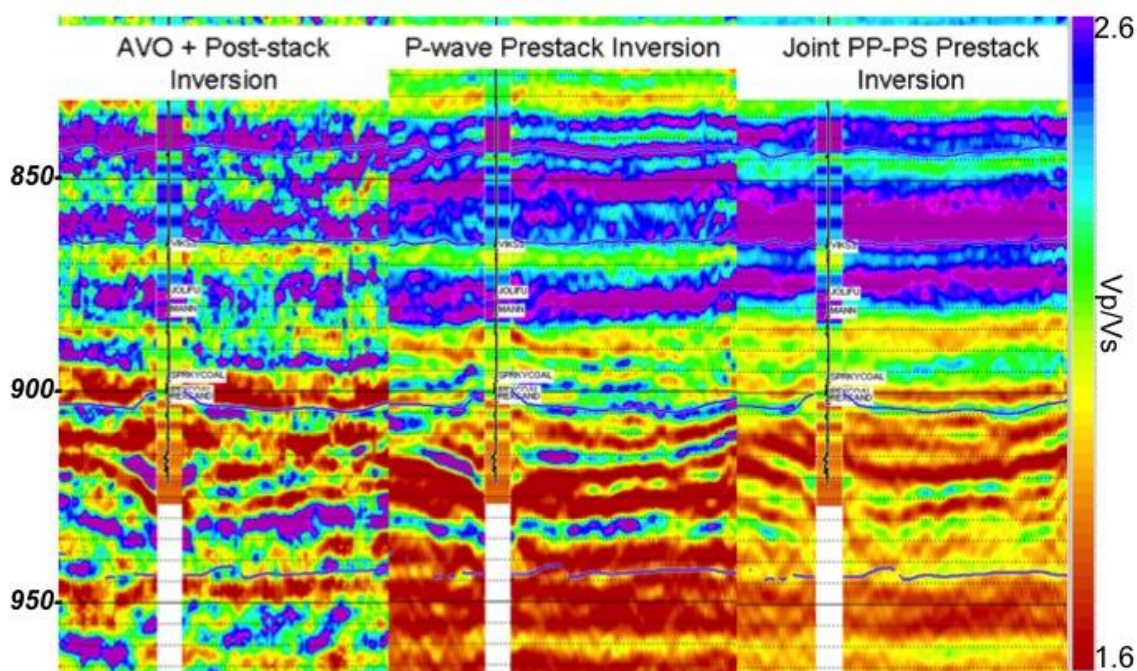
content of the converted-wave data. A cross-section of the  $V_p/V_s$  calculated via joint simultaneous prestack inversion is shown in Figure 3.12, with the  $V_p/V_s$  from the time-depth relationship inserted for comparison.



**Figure 3.12:  $V_p/V_s$  from joint prestack inversion.  $V_p/V_s$  from logs at Well D has been inserted in colour and the SP log as the trace.**

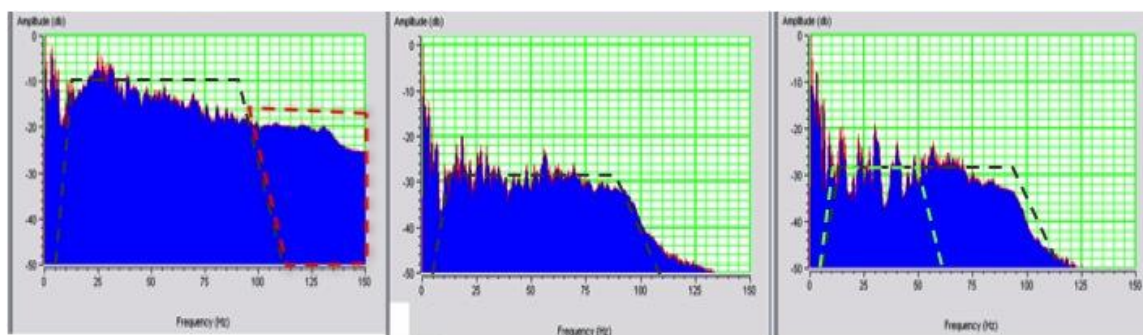
### 3.4 Discussion – seismic data

Figure 3.13 shows a comparison of the three different  $V_p/V_s$  methods for the same cross-line. Inserted into each section is the  $V_p/V_s$  calculated from depth-time relationships for comparison. We first observe that each of these volumes has different frequency content.



**Figure 3.13: Comparison of  $V_p/V_s$  calculated from AVO + poststack inversion (left), prestack inversion (middle) and joint prestack inversion (right).  $V_p/V_s$  from logs at Well D has been inserted in color and the SP log as the trace.**

The amplitude spectra of the  $V_p/V_s$  volumes are displayed in Figure 3.14. Given that the P-wave seismic data in all cases was filtered with the same bandpass parameters it is interesting to note the differences in the spectra.



**Figure 3.14:** Amplitude spectra of the Vp/Vs volumes taken from 10 inlines around well F. The left image shows the amplitude spectrum from the AVO + poststack inversion has significantly more high frequency noise (red outline) from the inversion than either, the prestack inversion (middle) or the joint prestack inversion (right), and higher frequencies higher than the filter applied to the PP-gathers. Also, the joint prestack inversion does show notches in its spectrum over the converted wave bandwidth (green dashed line). Horizontal axes extends from zero to 150 Hz and the vertical axes from -50 to 0 dB-down.

Comparing the wavelets (near against Rp, and far against Rs), we note some differences, particularly at the high frequencies on the Rs wavelet (Figure 3.15). It would appear that the weighted stacking process of AVO has preserved more high-frequency energy than is present on the individual angle stacks. As the input data did not contain this frequency content, due to filtering, it must be the result of inversion noise contaminating the resulting Vp/Vs.

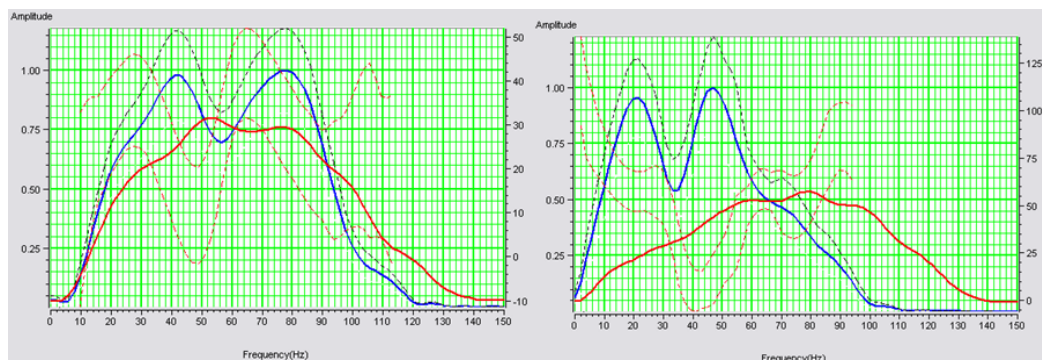


**Figure 3.15:** Amplitude spectra of the wavelet used in the inversions. The left image shows a comparison of the near angle wavelet (blue) with the wavelet used to invert the P-wave reflectivity (red). A similar comparison is shown for the far angle (blue) and the S-reflectivity wavelet (red).

Interestingly, by going back one step to look at the amplitude spectra on the impedance volumes, the high frequencies on these attributes are much more suppressed (Figure 3.16).

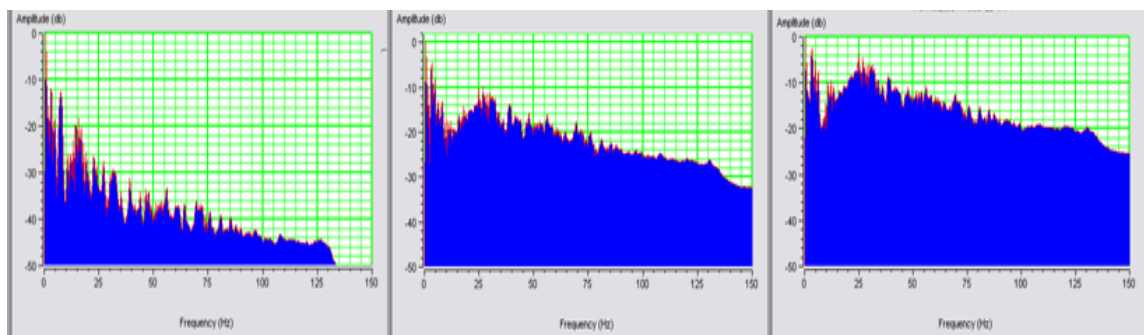


**Figure 3.16: Amplitude spectra of the attributes derived from the AVO + poststack inversion flow. The left image shows the spectrum from the P-Impedance, the middle from the S-Impedance, and the spectrum from the Vp/Vs is on the right. Taking the ratio of the impedances has enhanced the high-frequency content of the data, likely by introducing noise.**

It is possible that we have accidentally demonstrated one of the potential pitfalls with the AVO + poststack inversion technique. That pitfall is that while the inversion is running it is minimizing the error on the reflectivity estimates by iteratively changing the reflectivity of each sample. Since the inversion for P-Impedance and S-Impedance are decoupled, we may have a situation where the P-wave inversion may put a reflector at sample  $x$ , but that same geologic event may occur on the S-wave inversion at sample  $x-1$  or  $x+1$ . When we then ratio these two attributes which contain alignment errors, we produce high-frequency artefacts (see Figure 3.17).

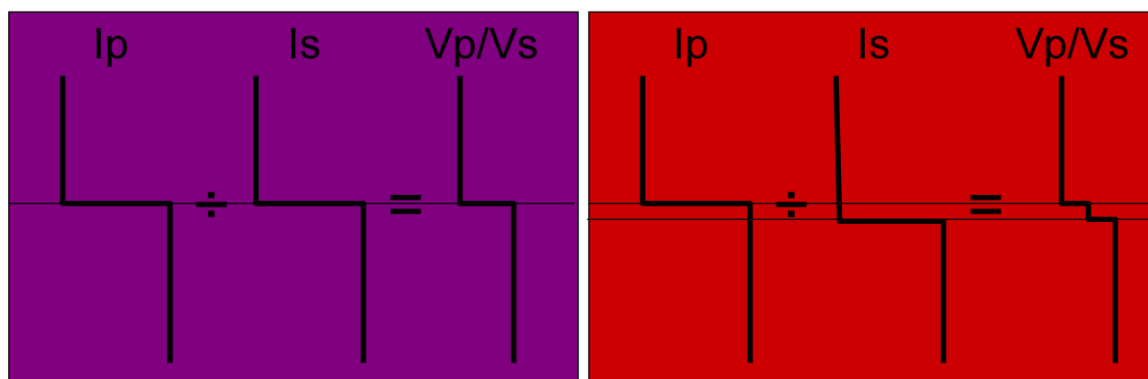


**Figure 3.17: Cartoon representation of the idealized (left) and realized (right) boundaries from the independent poststack inversions. The left image shows the idealized case where the bed-boundaries occur coincident on the P- and S-Impedance inversions. The right image shows what has occurred to contribute the high-frequency noise to the resulting Vp/Vs volume, in which the bed-boundaries occur on different samples, resulting in high-frequency jitter imparted to the Vp/Vs volume.**

Examining the amplitude spectrum of the joint prestack inversion, we can see that using a cut-off of approximately 30 dB-down, there appears to be a large number of notches in the resulting amplitude spectrum (Figure 3.14c). While spectral notches can occur due to processing or acquisition issues (e.g. multiples; Margrave, 2007) the input data to the inversions does not possess these notches. It is therefore assumed that these spectral-notches are an artefact of the inversion process. Interestingly, these notches occur where the amplitude spectra of the P-wave and converted-wave data overlap in the frequency domain (Figure 3.14), from approximately 10 Hz to 50 Hz. One possible explanation is that there are errors present in the converted-wave registration such that the geology on each volume effectively does not align, causing the inversion to solve for two different geologies at the same time, which cannot be done, except at certain frequencies where tuning or some other effect allows for a solution to exist, though this

solution may still be non-geologic. The frequencies above the converted-wave band (i.e., > 50 Hz) are unaffected as the only data contributing to a solution at those frequencies is the P-wave data. Further work on registration may help to improve these results.

Another possible explanation, is the registration process has made the wavelet on the registered converted-wave data non-stationary in time (and possibly space). This result comes from different portions of each converted-wave trace being compressed a different amount, depending upon the Vp/Vs used for registration. This non-stationary wavelet violates one of the assumptions of the inversion process and, as a result, the amplitude spectrum of the inverted result is impacted within this frequency range.

The prestack inversion using P-wave data only, appears to be a good compromise between the high frequency noise of the AVO + poststack inversion and the relatively low frequency result using the joint prestack inversion. Additionally, the Vp/Vs result from the prestack inversion appears to give the most laterally continuous inversion result which also appears to correlate with well control. One way to determine this is to plot the inverted results at the well locations over the Vp/Vs from well logs. Figure 3.18 shows the Vp/Vs from four well location. Correlations between the Vp/Vs from filtered well logs and the various inversion results were calculated and displayed in figure 3.19, showing that averaging over four blind wells, the best correlation between the inversion and the well logs comes from the prestack inversion with a correlation of 69%, followed by the joint prestack inversion at 55% and then AVO + poststack inversion at a disappointing 46%.

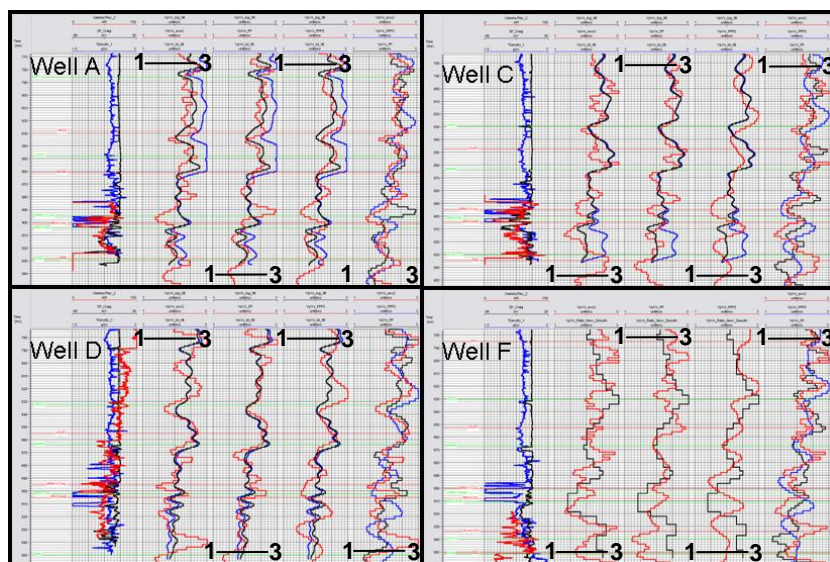


**Figure 3.18: Detailed trace comparisons for Vp/Vs extracted using on of the three methods discussed above for four wells. The left track shows the Gamma Ray (0-150 API, red), SP (-90 - +30, black) and Density (1.5-3.0 g/cc, blue) logs from the wells where the remaining tracks are comparisons to the various inversions (scale= 1.0 – 3.0) in the order in which they were completed, AVO + poststack inversion, prestack inversion, joint prestack inversion (black=log Vp/Vs, red=inversion, blue=depth-time). The 5<sup>th</sup> track compares each method directly.**

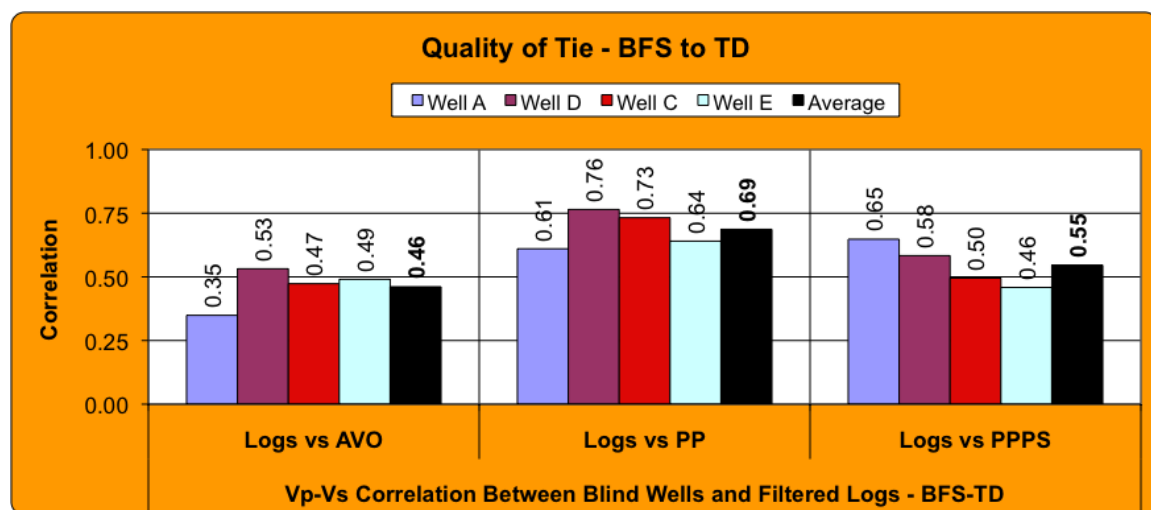


**Figure 3.19: Comparison of the correlation between Vp/Vs from filtered well logs and the various inversion results between the Base Fish Scales (BFS) to the base of the logs. Note the best results are coming from the prestack inversion (Logs vs. PP).**

While all three methods discussed in this work do assume small reflectivities (i.e.  $R(\theta) < 0.1$ ), the AVO + poststack inversion has this assumption built into each of the two inversion steps. Because the assumption is violated in the geology surrounding the target interval, it is possible that the error introduced by making this assumption is exasperated in the second inversion, resulting in the poor results shown in the examples shown here in the AVO + poststack inversion workflow. This is true of all three inversion methods mentioned above. Because the reflectivity contrast of the coals is so high, approaching ten times higher than the average background reflectivity (Figure 3.20), this assumption is violated and the solution at that level is therefore left in doubt.

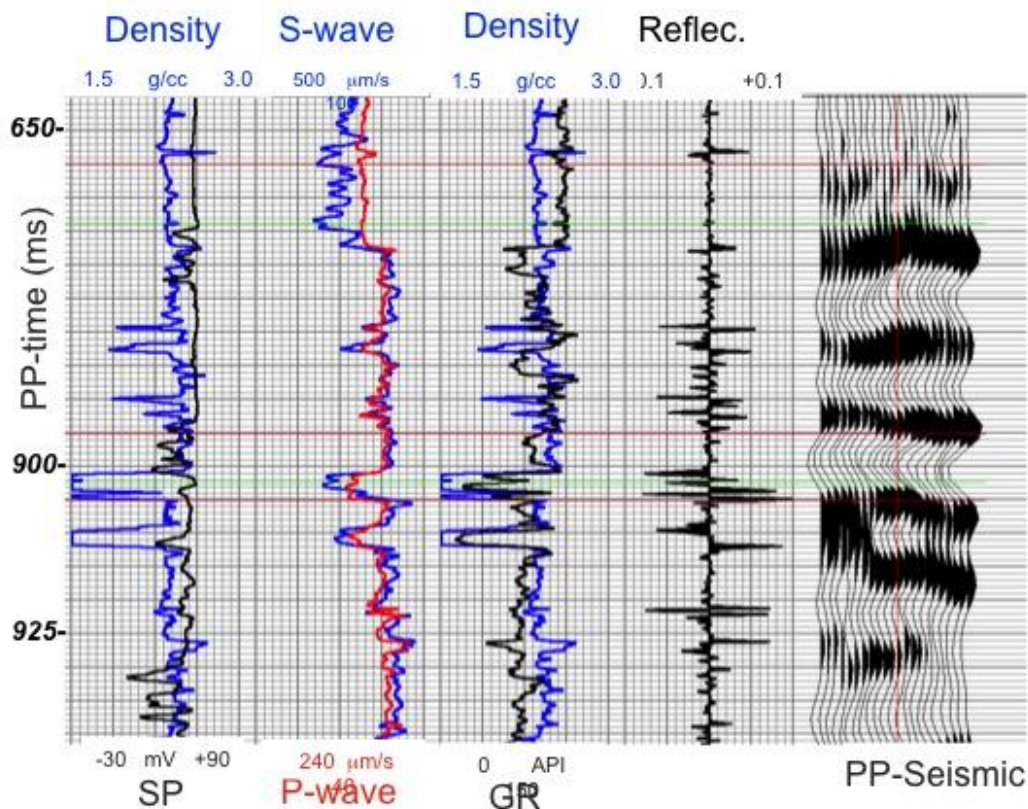


**Figure 3.20: Plot of well logs for well D. Reflectivity is plotted in the 4<sup>th</sup> track and shows that the small reflectivity assumption is violated by the coals.**

## Chapter Four: **Conclusions**

In summary, three different inversion methods were tested and evaluated based upon their ability to estimate  $V_p/V_s$  from well logs data.

1. Amplitude variation with offset (AVO) with two poststack inversions
2. Prestack inversion of P-wave data only
3. Joint-prestack inversion of P-wave and converted-wave data

Based upon the results presented here, AVO + poststack inversion produces the least favourable (i.e. worst well tie and most noise) result and the prestack inversion of P-wave data appears to be the best method to estimate  $V_p/V_s$  from seismic data; however, future work could impact these results. Similar analysis on model data suggest that while joint prestack inversion should have produced the best estimate of  $V_p/V_s$ , the inversion results can be sensitive to even very small registration errors. A combination of small registration errors and isotropic processing may have contributed to the degradation of the results from joint prestack inversion.

Reprocessing the converted-wave data to account for shear wave birefringence may significantly improve the amplitude correlation in addition to the frequency content of the converted-wave data. It may be possible to better register this data (e.g. prestack depth migration), thereby improving the accuracy of both the registration and the joint prestack inversion. Anderson and Larson (2006) showed that converted-wave traveltime delays as large as 30 ms are present on this data, therefore this is expected to have a significant impact on both the amplitude and frequency content of the converted wave data. Additionally, more detailed registration work, or even prestack depth migration of both PP and PS data, may better align geology between the P-wave and converted-wave

volumes, resulting in better joint inversions. Dipole sonic logs are a critical component of registering PS-data to PP-time and should be acquired whenever possible.

Incorporation of the Vp/Vs from registration into each inversion could improve all three inversion techniques. Revised processing of the P-wave data to incorporate larger offsets/angles may help to constrain the inversion results, perhaps even allowing an inversion for density, however this would require higher-order move-out corrections or other brute-force methods (e.g. time-variant trim static).

We have observed that the AVO + poststack inversion flow has potential pitfalls which appear to have been encountered with this data set due to the fact that we are solving for related parameters in an unrelated fashion, resulting in artefacts (high-frequency noise on subsequent products like Vp/Vs). Registration of the converted-wave data violates the “stationary wavelet” assumption inherent in the inversion process. Additional research is needed, however, in order to find a method to resolve this non-stationarity. Caution should also be exercised when estimating rock properties from seismic data that contains geology which violates any of the assumptions used in the rock properties extraction. Based upon the results shown to date, the prestack (P-wave only) inversion appears to have produced the best correlation to well control with a relatively small amount of noise generated as a result of the inversion process.

Future work on this data should include reprocessing of the PP-seismic data to improve normal moveout correction so as to allow for larger incident angles to be included in the inversions discussions contained herein. Extending the angles would allow better constrain the inversion and may even allow for reliable inversion of both density reflectivity and density inversion. Additionally, it has been shown that horizontal

transverse isotropy (HTI) has severely impacted the quality of the converted wave seismic data (figure 4.2) by inducing azimuthally dependant time-delays to the reflections. Anderson and Larson (2006) have shown these time-delays to be very large (i.e.  $> 25$  ms), and as such have limited the frequency content and amplitude fidelity of the PS-seismic data. Not only do the amplitude distortions and time delays cause problems for the joint prestack inversion, but properly accounting for this effect in processing could provide a means of deriving a more detailed  $V_p/V_s$  model for registration, removing at least some of the errors involved in registering the PS-data to PP-time.

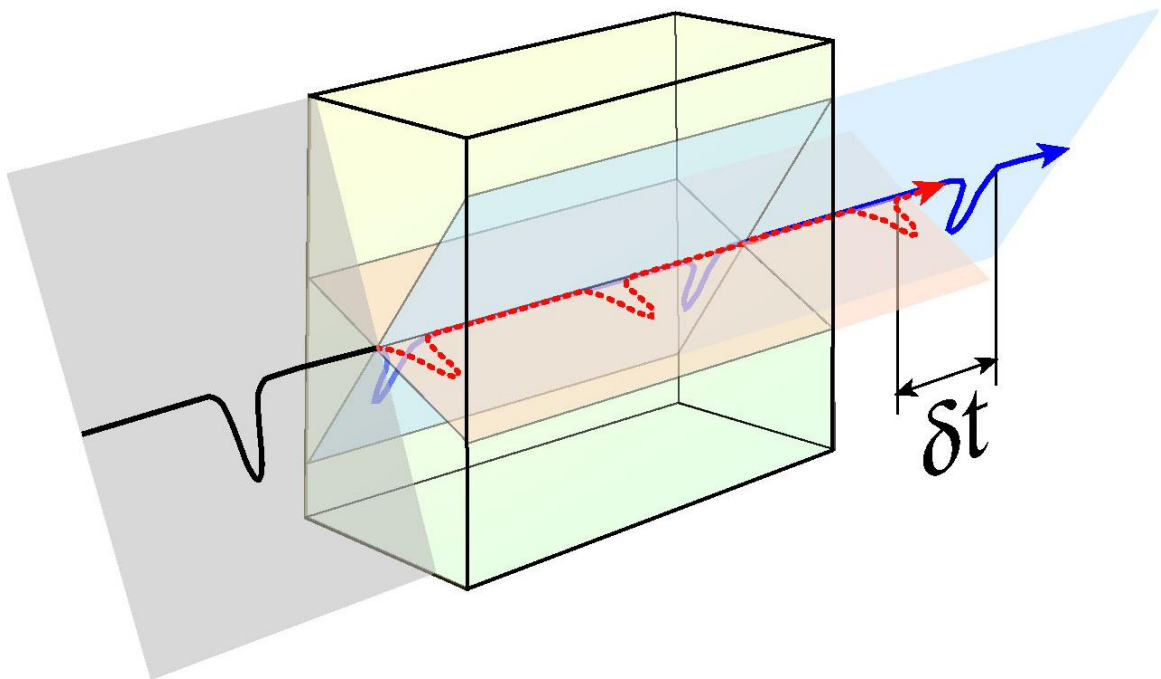


**Figure 4.1: Cartoon description of shear-wave splitting.** If the mechanism of splitting is aligned along a single azimuth, the time-delay ( $\delta t$ ) can be azimuthally variant (from <http://garnero.asu.edu>).

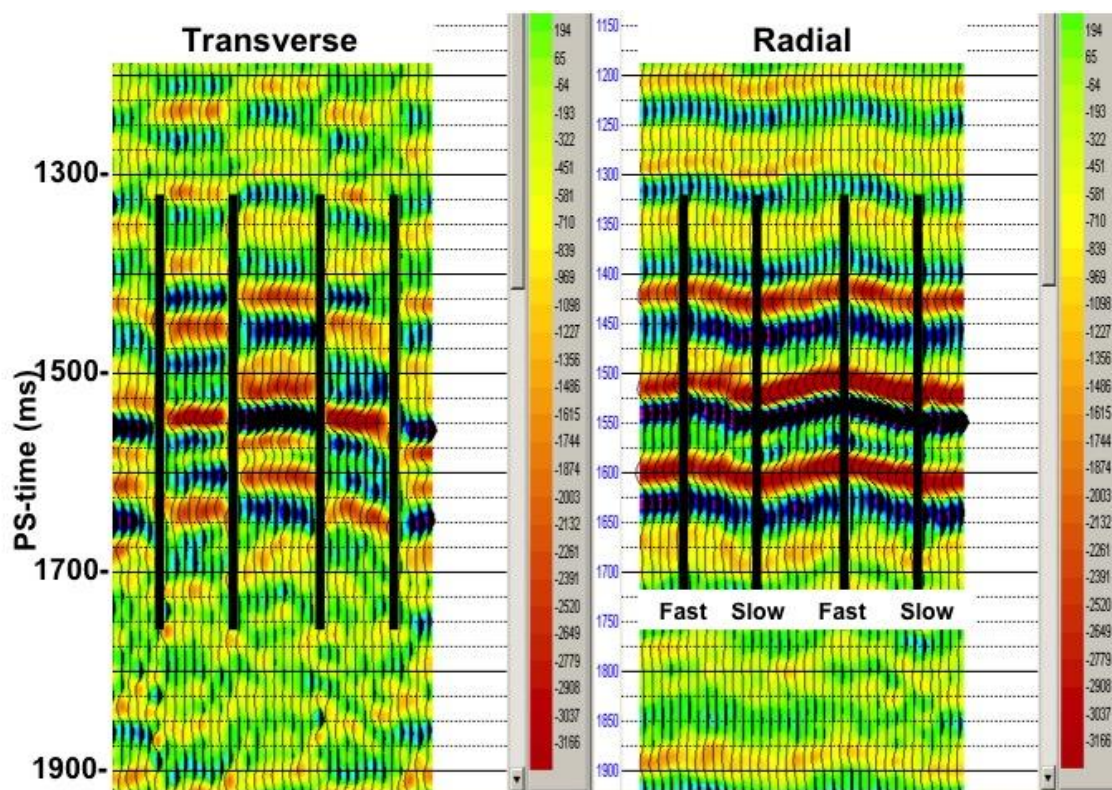


**Figure 4.2: Example of shear-wave splitting as evidenced on the seismic data used in this study. The left image shows the transverse component of the converted wave data at a single CCP, stacking along different azimuths. The right image shows the same CCP location and the characteristic time delay associated with the fast and slow azimuths. The phase reversals on the transverse section coincides with the fast and slow azimuths on the radial section, providing strong evidence of shear wave splitting. Note that the traveltime differences of approximately 20 ms shown on the radial data above were not removed prior to stacking, impacting both the amplitudes and frequency content of the radial volume.**

As previously mentioned, other authors have performed joint prestack inversion analysis by using prestack depth migration for both the PP- and PS-datasets, allowing for the processing to register the data by processing with a unified Earth model. Comparing joint prestack inversion results between registration by prestack depth migration against horizon based registration would also be of value.

## Chapter Five: **References**

- Agullo, Y., D. Macé, K. Labat, T. Tonellot, A. Bourgeois, and M. Lavielle, 2004, Joint PP and PS stratigraphic inversion for prestack time migrated multicomponent data, 74<sup>th</sup> Ann. Internat. Mtg.: Soc. Expl. Geophys., Expanded Abstracts
- Aki, K. and P.G. Richards, 1980, Quantitative Seismology, v. 1, sec 5.2
- Anderson, P. F., and R. Larson, 2006, Multicomponent case study - One company's experience in Eastern Alberta: Recorder, 31, 5–10.
- Aster, R.C., B. Borchers, and C.H. Thurber, 2005, Parameter Estimation and Inverse Problems, Elsevier Academic Press
- Castagna, J.P., M.L. Batzle, and R.L. Eastwood, 1985, Relationships between compressional-wave and shear-wave velocities in clastic silicate rocks: Geophysics, **50**, 571 – 581
- Castagna, J.P. and M. Backus, 1993, Offset-dependent reflectivity, SEG Publication, Tulsa, Ok.
- Downton, J., 2005, Seismic parameter estimation from AVO inversion, PhD Thesis, University of Calgary
- Fatti, J.L., G.C. Smith, P.J. Vail, P.J. Strauss, and P.R. Levitt, 1994, Detection of gas in sandstone reservoirs using AVO analysis: A 3-D seismic case history using the Geostack technique. Geophysics, 59, 1362-1376.
- Gaiser, J., 1996, Multicomponent Vp/Vs correlation analysis: Geophysics, 61, no. 4, 1137 - 1149
- Gardner, G.H.F., L.W. Gardner, A.R. Gregory, 1974, Formation velocity and density – the diagnostic basics for stratigraphic traps: Geophysics, **39**, 770 – 780

- Gidlow, P. M., G.C. Smith, and P.J. Vail, 1992, Hydrocarbon detection using fluid factor traces, a case study: How useful is AVO analysis? Joint SEG/EAGE summer research workshop, Technical Program and Abstracts, 78-89.
- Goodway, B., T. Chen, and J. Downton, 1997, Improved AVO fluid detection and lithology discrimination using Lamé petrophysical parameters; ' $\lambda\rho$ ', ' $\mu\rho$ ', and ' $\lambda/\mu$  fluid stack' from P and S inversions, 67th Ann. Internat. Mtg: Soc. of Expl. Geophys., 183-186.
- Hampson, D. P., B. H. Russell, and B. Bankhead, 2005, Simultaneous inversion of pre-stack seismic data: 75th Annual International Meeting, SEG, Expanded Abstracts , 1633-1637.
- Hilterman, F., J.W.C. Sherwood, R. Schellhorn, B. Bankhead, B. DeVaurt, 1996, Detection of hydrocarbons with lithostratigraphy, 66<sup>th</sup> Ann. Internat. Mtg.: Soc. Expl. Geophys., Expanded Abstracts
- Knapp, S., T. Medley, C. Behtaz, R. Uden, and F. Henery, 2002, Inversion of PP and PS multicomponent seismic volumes: a case history from the Gulf of Mexico, 72<sup>nd</sup> Ann. Internat. Mtg.L Soc. Expl. Geophys., Expanded Abstracts, 1042-1044
- Larsen, J., 1999, AVO Inversion by simultaneous P-P and P-S Inversion, M.Sc. Thesis, University of Calgary
- Lindseth, R.O., 1979, Synthetic sonic logs – a process for stratigraphic interpretation, Geophysics, **44**, 3 – 26
- Lines, L.R., and R.T. Newrick, 2004, Geophysical Monograph Series: Fundamentals of Geophysical Interpretation no. 13, SEG Books

- Ma, X., 2002, Simultaneous inversion of prestack seismic data for rock properties using simulated annealing, *Geophysics*, **67**, no. 6, pp 1877-1885
- Margrave, G., R. Stewart and J. Larsen, 2001, Joint PP and PS seismic inversion: The Leading Edge, 20, no. 9, 1048 - 1052
- Ostrander, W. J., 1984, Plane-wave reflection coefficients for gas sands at nonnormal angles-of-incidence: *Geophysics*, 49, no.10, 1637-1648
- Pendrel, J., H. Debeye, R. Pedersen-Tatalovic, B. Goodway, J. Dufor, M. Bogaards, R. Stewart, 2000, Estimation and interpretation of P- and S-impedances from simultaneous inversion of P-wave offset seismic data, 70<sup>th</sup> Ann. Internat. Mtg.: Soc. Expl. Geophys., Expanded Abstracts, 146-149
- Russell, B., 1988, Introduction to Seismic Inversion Methods, SEG Course Notes Series, Volume 2
- Sheriff, R.E., 2002, Encyclopedic Dictionary of Exploration Geophysics, Society of Exploration Geophysicists
- Shuey, R.T., 1985, A simplification of the Zoeppritz equations, *Geophysics*, **50**, no. 4, 609 - 614
- Smith, G.C., and P.M. Gidlow, 1987, Weighted stacking for rock properties estimation and detection of gas: *Geophysical Prospecting*, **35**, 993 – 1014
- Stewart, R., 1990, Joint P- and P-SV inversion, CREWES Research Report, 3, 112 – 115
- Stewart, R., J. Gaiser, R. Brown, D. Lawton, 2002, Converted-wave seismic exploration: Methods: *Geophysics*, 67, no.5, 1348 - 1363
- Veire, H. and M. Landro, 2006, Simultaneous inversion of PP and PS seismic data: *Geophysics*, 71, no. 3, R1 – R10

- Verm, R. and F. Hilterman, 1995, Lithology color-coded seismic sections: The calibration of AVO crossplotting to rock properties, *The Leading Edge*, **14**, 847 - 853
- Wallace, R., and R. Young, 1996, Pre-stack Inversion: Evolving the Science of Inversion, *Recorder*, **21**, no. 10, pg. 3
- White, R., 1997, The accuracy of well ties: Practical procedures and examples. 67th Annual International Meeting, *SEG Expanded Abstracts*, 816
- Widess, M.B., 1973, How Thin is a Thin Bed, *Geophysics*, **38**, no. 6, pp 1176 – 1180
- Young, G.R., and M.K. Sen, 2007, A comparison of porosity estimates obtained using post-, partial-, and prestack seismic inversion methods: Marco Polo Field, Gulf of Mexico. 77<sup>th</sup> Ann. Internat. Mtg.: Soc. Expl. Geophys., *Expanded Abstracts*
- Yilmaz, O. and S.M. Doherty, 2001, *Seismic Data Analysis: Processing, Inversion and Interpretation of Seismic Data*, Second Edition, SEG Publication, Tulsa, Ok.

## **APPENDIX A: PP SEISMIC DATA PROCESSING FLOW**

The following is a summary of the processing sequence followed on the PP-gathers, up to and not including the inversions performed in this thesis. While processing was performed by multiple contractors, the version of processing used was completed in 2006 by Veritas GeoServices Ltd. (now CGGVeritas). Where known, the name of the algorithm within Veritas' software has been identified in brackets.

1. Reformat
2. 3D Geometry
3. Amplitude Recovery:
4. Manual Trace Edits
5. Coherent Noise Attenuation (CNA)
6. Despiking (BLAST)
7. Surface Consistent Deconvolution
8. Near Surface Structure Statics – 2-layer drift calculation
9. Trace Gather:
10. Preliminary Velocity Analysis:
11. Surface consistent Residual Statics (MASTT)
12. Spectral Whitening (SPECBAL)
13. Surface Consistent Scaling
14. Final Velocity Analysis
15. Surface Consistent Residual Statics (MASTT)
16. CMP Trim Statics (TRIM)
17. Mute

18. Prestack Scaling

19. Bandpass Filter

20. Prestack Scaling

## **APPENDIX B: PS SEISMIC DATA PROCESSING FLOW**

The following is a summary of the processing sequence followed on the PS-data, up to and not including the inversions performed in this thesis. While processing was performed by multiple contractors, the version of processing used was completed in 2006 by Veritas GeoServices Ltd. (now CGGVeritas). Where known, the name of the algorithm within Veritas' software has been identified in brackets.

1. Reformat
2. 3D Geometry
3. Amplitude Recovery:
4. Coherent Noise Attenuation (CNA)
5. Despiking (BLAST)
6. Surface Consistent Deconvolution
7. Apply Shot-Component Structure Statics (see Appendix A)
8. Trace Gather for PS-data (Asymptotic Conversion Point)
9. Preliminary Velocity Analysis
10. Surface Consistent Residual Statics (MASTT)
11. Final Velocity Analysis
12. INVEST Noise Attenuation
13. Spectral Whitening
14. Mute
15. Trace Scaling
16. Long Wave Structure Statics (estimated)
17. Trim Statics (TRIM)

18. CCP Velocity Analysis
19. CCP Binning
20. Stack
21. FXY Noise Attenuation
22. Poststack Migration
23. Spectral Shaping (ZSIGNAL)
24. Phase Correction
25. Filter
26. Trace Scaling